Feasibility study of ultrasonic inspection of thin laser welds on fuel cell bipolar plates

by

Geoffrey VEIT

THESIS PRESENTED TO ÉCOLE DE TECHNOLOGIE SUPÉRIEURE
IN PARTIAL FULFILLEMENT FOR A MASTER'S DEGREE
WITH THESIS IN AUTOMATED MANUFACTURING ENGINEERING
M. A. Sc.

MONTREAL, JULY 23, 2019

ÉCOLE DE TECHNOLOGIE SUPÉRIEURE
UNIVERSITÉ DU QUÉBEC

BOARD OF EXAMINERS

THIS THESIS HAS BEEN EVALUATED

BY THE FOLLOWING BOARD OF EXAMINERS

Prof. Pierre Bélanger, Thesis Supervisor
Department of mechanical engineering at École de technologie supérieure

Prof. Catherine Laporte, President of the Board of Examiners
Department of electrical engineering at École de technologie supérieure

Prof. Tan Pham, Member of the jury
Department of mechanical engineering at École de technologie supérieure

THIS THESIS WAS PRESENTED AND DEFENDED

IN THE PRESENCE OF A BOARD OF EXAMINERS

ON JULY 4, 2019

AT ÉCOLE DE TECHNOLOGIE SUPÉRIEURE

ACKNOWLEDGMENT

I first would like to thank my thesis advisor, Pr. Pierre Belanger for his dynamism and expertise throughout this project. His advices have always been right and helpful. It was a pleasure to work with him as a real partner with his full confidence.

Besides my adviser, I would like to make a warm thanks to all the members of Pulets: Sevan, Nicolas, Arthur, Baptiste, Anthony, Frédéric, Guillaume, Aurélien, Thibault, Damien, Aubin, Cherif, Daniel and Mathieu. Thank you for making such a fantastic atmosphere in the lab.

This project was made possible thanks to our industrial partner Mercedes-Benz Fuel Cell. A special thanks to Dr. Taryn Biggs and Dr. Thomas Maassen for their support during this project.

This project would not have been possible without the collaboration between my engineering school in France Arts & Métiers ParisTech, École de Technologie Supérieure and the agreements between our great countries. Therefore, thank you to all the people involved in the preservation and development of these relationships.

I must express my very profound gratitude to Nolwenn Cousin for her love, support, patience, and understanding.

Finally, I would like to thank with all my heart my family for their unconditional support. Their curiosity, open mind and readiness to learn have always inspired me. Bon vent et bon vol.

Étude de faisabilité sur l'inspection de fines soudures laser de piles à hydrogène

Geoffrey VEIT

RÉSUMÉ

Dans une optique de démocratisation des véhicules à hydrogène, l'industrie automobile travaille sur le développement et le perfectionnement des procédés de fabrication afin de lancer une production de masse. Par soucis d'optimisation des couts et du poids, certains composants des piles à combustible hydrogène ont été fortement réduits en épaisseur. C'est notamment le cas des plaques bipolaires qui composent les piles à membrane échangeuse de protons. Les plaques bipolaires se composent de deux fines plaques d'acier inoxydable soudées par laser en de nombreux points. Cependant, les soudures laser montrent des défauts internes pouvant mener à des fuites internes ou externes. Ainsi, le développement d'une méthode d'évaluation non destructive et fiable pour évaluer l'intégrité structurelle des soudures laser de très petites dimensions sur les plaques bipolaires des piles à hydrogène est indispensable. La méthode doit pouvoir déterminer les joints défaillants et décrire les caractéristiques du défaut. Les méthodes d'inspection de soudures laser sont nombreuses et variées. Cependant, aucune n'a été évaluée pour inspecter des défauts internes dans des soudures de si faibles dimensions (environ 200 µm de largeur). Ce mémoire se concentre sur les solutions ultrasonores qui pourraient être apportées afin de répondre à cette problématique. Les ultrasons ont l'avantage sur les autres techniques de contrôle non destructif de pouvoir inspecter la structure interne des soudures, de pointer la position de défauts et pouvoir caractériser ceux-ci.

Deux méthodes de contrôle par ultrasons ont été menées dans ce mémoire : le contrôle par ondes guidées ainsi que la microscopie acoustique. Chacune de ces méthodes a été évaluée dans un premier temps par un modèle d'éléments finis afin de simuler l'émission et la propagation de l'onde ultrasonore au travers des divers milieux transverses. Ces simulations ont permis de démontrer la faisabilité et les limites des méthodes. L'analyse des défauts pouvant se trouver dans les soudures a ainsi été réalisée. Par la suite, des expérimentations ont été menées sur plusieurs échantillons présentant diverses géométries et défauts. À la lumière des résultats obtenus, une conclusion sur la faisabilité de l'inspection par ultrasons de fines soudures laser des plaques bipolaires ainsi que des pistes d'amélioration pour les travaux futurs ont été formulées.

Mots-clés : Ondes ultrasonores, Plaque bipolaire, Soudure laser, Acier inoxydable

Feasibility study of ultrasonic inspection of thin laser welds on fuel cell bipolar plates

Geoffrey VEIT

ABSTRACT

With a perspective of democratizing hydrogen-powered vehicles, the automotive industry is working on the improvement of the manufacturing processes with the aim to launch mass production. In order to optimize costs and weight, some hydrogen fuel cell components have been significantly reduced in thickness. This is especially true for the bipolar plates of the proton exchange membrane fuel cells. They consist of two thin stainless steel laser welded plates. However, laser welding may lead to internal defects, which can cause internal or external leaks. Thus, the development of a nondestructive and reliable evaluation method to assess the structural integrity of very thin laser welds on bipolar plates of hydrogen fuel cells is essential. The method must be able to identify the failed joints and describe the characteristics of the failure. Laser weld inspection methods are many and varied. However, none have been evaluated to inspect internal defects in such small welds (about 200 μm wide). This thesis focuses on ultrasonic solutions that could address this issue. Ultrasonic testing has the advantage over other nondestructive testing techniques of being able to inspect the internal structure of welds by locating and characterizing defects.

Two ultrasonic inspection methods were investigated in this thesis: ultrasonic guided waves and acoustic microscopy. The methods were first evaluated using finite element simulation of the emission and propagation of the ultrasonic waves through the various transverse media. These simulations demonstrated the feasibility and limitations of the methods. The analysis of defects that may be found in the welds was thus carried out. Subsequently, experiments were carried out on several samples with various geometries and defects. Based on the results obtained, a conclusion on the feasibility of ultrasonic inspection of fine laser welds on bipolar plates and possible improvements for future work were formulated.

Keywords: Ultrasonic waves, Bipolar plates, Laser welding, Stainless steel

TABLE OF CONTENTS

LIST OF FIGURES

Page

LIST OF ABREVIATIONS

BiP	Bipolar Plates
FE	Finite Element
FFT	Fast Fourier Transform
GW	ultrasonic Guided Waves
NDT	Nondestructive Technique
SAFT	Synthetic Aperture Focusing Technique
SAM	Scanning Acoustic Microscopy
TFM	Total Focusing Method
μCT	Micro Computed Tomography
1-D	One-Dimension
2-D	Two-Dimensions
3-D	Three-Dimensions

LIST OF SYMBOLS

δ_{ij}	Kronecker delta
u	Vector of displacement
Λ	First Lamé parameter
t	Time
$\frac{\partial}{\partial}$	Partial derivative
ρ	Density
μ	Second Lamé parameter
E	Young's modulus
G	Shear modulus
ν	Poisson's ratio
σ	Stress tensor
ε	Strain tensor
c	Bulk velocity
c_l	Longitudinal velocity
c_t	Transversal velocity
cos	Cosine function
sin	Sine function
tan	Tangent function
Hz	Hertz
m	Meter
s	Second

Pa	Pascal
dB	Decibel
V_{ph}	Phase velocity
V_g	Group velocity
Φ	Scalar potential
Ψ	Vector potential
M	Diagonal lumped mass matrix
K	Static stiffness matrix
C	Viscous damping matrix
F	External force vector

INTRODUCTION

The first fuel cells were invented at the beginning of the 19th century. The first commercial use of fuel cells came more than a century later with aerospace applications. Since then, fuel cells have evolved. They are used in more and more applications such as backup power units or in the automotive industry (Amphlett, Mann, Peppley, Roberge, & Rodrigues, 1996).

The proton exchange membrane fuel cell is a type of fuel cell that has been mainly studied in the last five decades. It comprises an anode, a cathode, and an electrolyte membrane (Appleby, 1988). It works by passing hydrogen through the anode and oxygen through the cathode. The hydrogen molecules are split into electrons and protons at the anode site. Then, the protons pass through the electrolyte membrane, while the electrons are forced through a circuit, generating an electric current and heat. At the cathode, the protons, electrons, and oxygen combine to produce water molecules. One recent configuration of fuel cell stack consists of combining the anode and cathode in a single component called a bipolar plate (BiP). The BiP supplies the gases through the flow channels to the electrodes. It also provides structural support for the membrane and facilitates water and heat management within the cell as the coolant flows through the BiP.

One common material of BiP is stainless steel, as these parts require high corrosion resistance, electrical conductivity, high mechanical strength, low weight and low costs, etc. In this project, BiP are composed of two stainless steel plates with a thickness around 100 μm that are formed, then joined with laser welds, and finally surface coated.

Unfortunately, when the coolant channels of the bipolar plates are pressurized, leaks can be observed. This can be a consequence of failed laser welds. Such leaks could for example cause a drop in performance and therefore must be understood.

Over the past few years, laser welding has been widely used in manufacturing from vehicle assembly in automotive production to the joining of microelectronic components in the

electronics industry due to its high speed, non-contact, high precision and low heat effects. Therefore, on-line monitoring techniques have been developed (Shao & Yan, 2005) in order to detect defective welds during manufacturing. Various methods were developed including acoustic emission (Farson & Kim, 1999), optical detectors (Sforza & de Blasiis, 2002), radiation sensors (Y. Zhang, Kovacevic, & Li, 1996), laser ultrasonics, and plasma charge sensors (Li, Brookfield, & Steen, 1996). To detect defects once the weld is completed, conventional NDT (Ditchburn, Burke, & Scala, 1996) such as visual inspection, radiographic inspection, ultrasonic testing, eddy current testing and magnetic particle testing can be used. However, most of these techniques are not suitable to detect defects in very thin welds (around 200 μm large) or are limited to volumetric defects. The only technology that seems to have these requirements is ultrasonic testing as it can detect non-volumetric defects and have a sufficient resolution.

The purpose of this project is, therefore, to find and characterize defective laser welds using ultrasonic non-destructive testing (NDT).

This thesis is divided in three chapters. The first will introduce the theoretical background of the propagation of ultrasonic waves and review the literature on the subject. Then two different approaches will be presented in the following chapters: ultrasonic guided waves (GW) in chapter 2 and scanning acoustic microscopy (SAM) in chapter 3. Both will be assessed using numerical models and experimental validation. Finally, conclusions will be drawn.

CHAPTER 1

THEORETICAL BACKGROUND AND LITERATURE REVIEW

In order to develop an ultrasonic NDT method for the detection of defects in thin laser welds, it is crucial to understand the fundamentals of the topics involved: ultrasonic wave propagation, GW, SAM and weld failures. Therefore, this chapter discusses the essential theoretical background of the ultrasonic bulk waves and GW in solids. Then, the geometry, important characteristics of BiP and the main defects induced by laser welding are discussed. Finally, GW, SAM inspection and fundamental imaging methods that are used in the thesis are presented.

1.1 Fundamentals of ultrasonic wave propagation

Ultrasonic waves have been extensively studied for over 300 years. The basic principles of ultrasonic waves are very well known and several textbooks discuss the topic (Cheeke, 2016; Krautkrämer & Krautkrämer, 2013; Rose, 2004). For this reason, an extensive review is omitted and only the essential theoretical elements are discussed in this section.

An ultrasonic wave can be defined as a stress or pressure oscillation propagating in a medium (gas, liquid, solid) at frequencies higher than the audible limit (20 kHz). There are many types of ultrasonic waves such as bulk waves, GW, surface waves (or Rayleigh waves), and many others.

1.1.1 Wave propagation in isotropic bulk media

Bulk wave corresponds to the propagation of waves in infinite isotropic media far from any boundaries. Bulk waves are separated in two main families: longitudinal or compressive waves and shear waves. The principal direction of displacement determines the kind of the wave. Figure 1.1 shows the deformation caused by longitudinal and shear waves in an unbounded

isotropic solid. Longitudinal waves propagate thanks to compression and dilatation of the material (Figure 1.1 a.) and shear waves propagates with the sliding of parallel and adjacent planes (Figure 1.1 b.). Shear waves can be polarized in two different directions for the same direction of propagation (vertical polarization: Figure 1.1 b. and horizontal polarization: Figure 1.1 c.).

Wave propagation was first theorized by d'Alembert for the one-dimensional case and later generalized to any three-dimensional case by Euler. The one-dimensional case highlights essential parameters associated to wave propagation such as the wavelength, wavenumber, period and angular frequency. The three-dimensional generalization brings an understanding of different modes of propagation that can be observed in the propagation of bulk waves. Euler provided a new vision of the different modes of bulk wave propagation. As Euler's formulation is generalized, only these equations will be developed.

The development of the equation of motion for an elastic isotropic solid is a classical topic covered in many textbooks (Graff, 2012). One way to derive these equations is to use Newton's second law for an elementary volume dxdydz:

$$\rho \frac{\partial^2 u_i}{\partial t^2} = \frac{\partial \sigma_{ij}}{\partial x_j} \tag{1.1}$$

where ρ is the density, u_i is the particle displacement along the i-axis and σ_{ij} is the stress tensor for an isotropic solid material defined by a generalization of Hooke's law:

$$\sigma_{kl} = c_{ijkl}\varepsilon_{kl} \tag{1.2}$$

where ε_{kl} is the strain tensor $\varepsilon_{kl} = \frac{1}{2}(\frac{\partial u_l}{\partial x_m} + \frac{\partial u_m}{\partial x_l})$, and c_{ijkl} is the stiffness tensor.

The stress tensor σ_{ij} can also be decomposed and written as:

$$\sigma_{ij} = \delta_{ij}\Lambda\varepsilon_{ii} + 2\mu\varepsilon_{ij} \tag{1.3}$$

where $\delta_{ij}=1$ if i=j, and $\delta_{ij}=0$ if i≠j. Λ and μ are Lame constants that define the normal elasticity E, the shear G and Poisson's ratio υ:

$$E = \frac{\mu(3\Lambda+2\mu)}{\Lambda+\mu}$$
$$G = \mu = c_{44} = \frac{c_{11}-c_{12}}{2} \tag{1.4}$$

$$\upsilon = \frac{\Lambda}{2(\Lambda+\mu)} = \frac{E}{2G} - 1$$

$$\Lambda = c_{12}$$

Using equations (1.4) in equation (1.3) we have:

$$\sigma_{ij} = c_{12}\delta_{ij}\varepsilon_{ii} + 2c_{44}\varepsilon_{ij} = (c_{11} - 2c_{44})\frac{\partial u_i}{\partial x_i}\delta_{ij} + c_{44}\left(\frac{\partial u_i}{\partial x_j} + \frac{\partial u_j}{\partial x_i}\right) \quad (1.5)$$

Finally, using equations (1.5) and (1.1):

$$\rho\frac{\partial^2 u_i}{\partial t^2} = \frac{\partial}{\partial x_i}\left((c_{11} - c_{44})\frac{\partial u_j}{\partial x_i}\right) + c_{44}\frac{\partial^2 u_i}{\partial^2 x_j} \quad (1.6)$$

This equation can be written in a vectorial form

$$\rho\frac{\partial^2 \vec{u}}{\partial t^2} = (c_{11} - c_{44})\vec{\nabla}\cdot\vec{\nabla}\cdot\vec{u}) + c_{44}\,\Delta\vec{u} \quad (1.7)$$

The three components of $\vec{u}$ can be uncoupled using the Helmholtz decomposition:

$$\vec{u} = \vec{\nabla}\Phi + \vec{\nabla}\times\Psi = \vec{u}_l + \vec{u}_t \quad (1.8)$$

where Φ is a scalar potential and Ψ a vector potential. $\vec{u}_l$ corresponds to the zero curl vector and $\vec{u}_t$ the zero divergence vector.

Two independent equations can then be determined using equation (1.7) and (1.8) :

$$\begin{cases} {c_l}^2\Delta\Phi - \frac{\partial^2\Phi}{\partial t^2} = 0 \\ {c_t}^2\Delta\Psi - \frac{\partial^2\Psi}{\partial t^2} = 0 \end{cases} \quad (1.9)$$

The first one corresponding to the longitudinal motion and depending on the scalar potential and the second one to a shear motion depending on the vector potential. Each motion is also characterized by a specific wave velocity: c_l for longitudinal wave velocity and c_t for shear wave velocity. The velocities are directly related to the material properties:

$$\begin{cases} c_l = \sqrt{\frac{\Lambda+2\mu}{\rho}} \\ c_t = \sqrt{\frac{\mu}{\rho}} \end{cases} \quad (1.10)$$

The demonstration shows the independent propagation of only two waves types in an isotropic and unbounded solid medium: longitudinal and shear waves. Any other wave propagation mode in a solid medium is derived from these two modes of propagation.

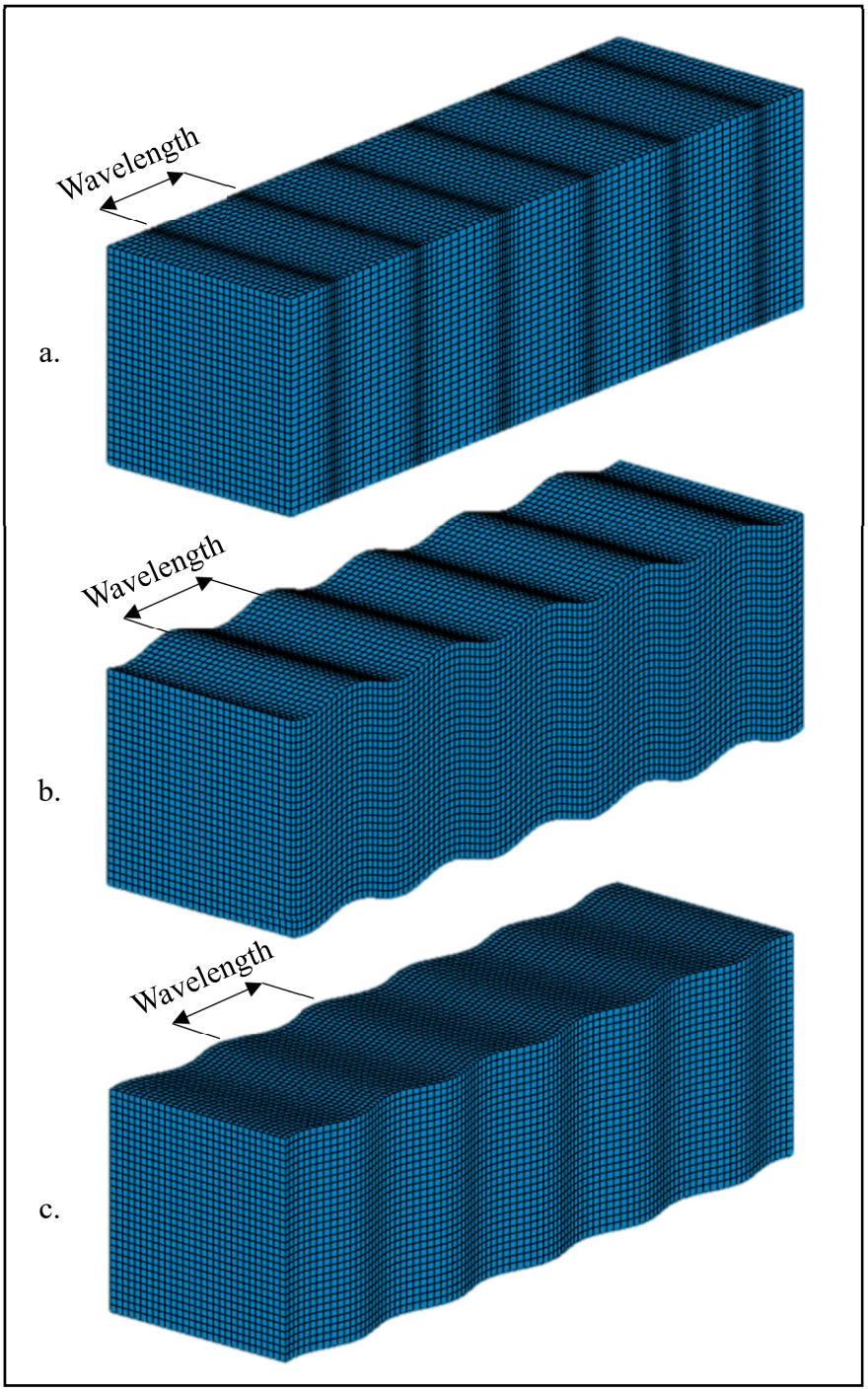

Figure 1.1 Deformations caused by the two longitudinal and shear waves in an unbounded solid. a. corresponds to a longitudinal wave. b. and c. correspond to shear waves polarized in two different directions, perpendicularly to the direction of propagation

1.1.2 Wave propagation in plates

General equations of propagation in infinite or semi-infinite media have been developed previously. In plates, the two boundaries generate multiple reflections of the wave. Therefore, specific modes of propagation can appear. These modes are known as GW modes. The propagation of elastic waves is well documented, and the development to obtain the wave equation is detailed by Rose in (Rose, 2014). Many types of GW exist: Lamb waves, shear horizontal waves, Love waves, Rayleigh waves. Only Lamb waves will be developed in this section, as they will be useful for the study.

Lamb waves are a complex case of propagation as they are generated from multiple constructive and destructive interferences between the longitudinal and the shear vertical waves. The interactions generate two types of particle motion: symmetric and antisymmetric modes. These solutions are often represented by dispersion curves of phase and group velocities as shown in Figure 1.2. These dispersion curves were obtained using the DISPERSE simulation tool (Pavlakovic, Lowe, Alleyne, & Cawley, 1997).

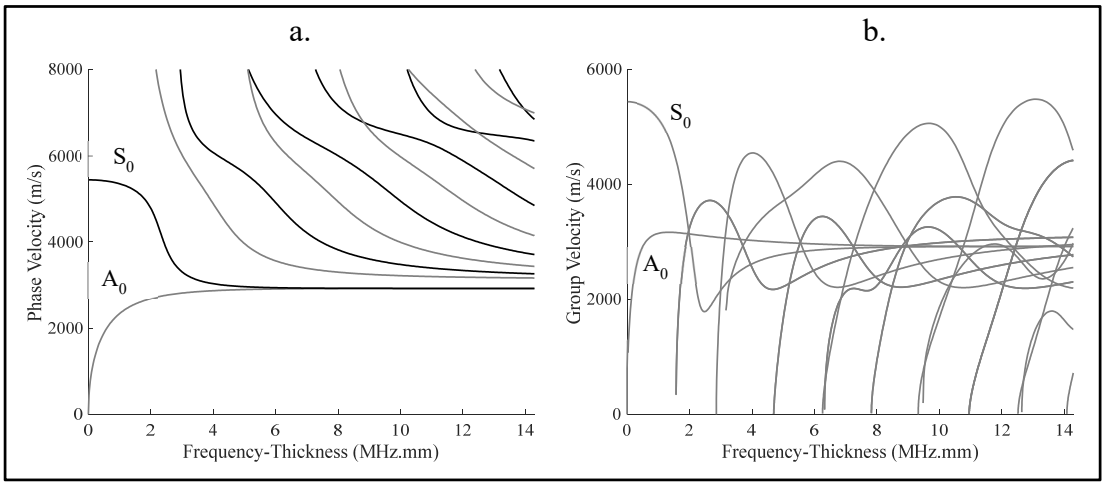

Figure 1.2 Dispersion curves of Lamb waves in an aluminum plate obtained with the DISPERSE simulation tool. a. Phase velocity dispersion curves. b. Group velocity dispersion curves

Lamb modes are dispersive (the group and phase velocities vary as a function of the mode, the thickness of the plate and the frequency). The high-order modes are characterized by a cutoff frequency. Moreover, the number of modes increases with frequency and some frequency bands contain modes that can be considered as virtually non-dispersive.

1.2 Finite element modelling of ultrasonic

There are many ways to simulate ultrasonic inspections. Main used softwares are based on Finite Element (FE) models such as Abaqus, COMSOL (Comsol, 2005) or Pogo (Huthwaite, 2014), or semi-analytical models such as CIVA (Calmon, Mahaut, Chatillon, & Raillon, 2006). Semi-analytical models can be useful for solving particular problems such as weld inspection with the use of wedge or bulk wave imaging. However, finite element models are more suited for the applications made in this thesis. Explicit and implicit FE models can be used to solve time domain wave propagation problems, However, explicit scheme has proved to be far more efficient than the implicit one (M. B. Drozdz, 2008).

FE simulations were conducted using Pogo (Huthwaite, 2014). Standard FE codes such as Abaqus or Ansys use Central Processor Units (CPU) and are rapidly limited in the number of degrees of freedom and execution time. Pogo uses Graphics Processor Units (GPU) that allow parallelization of the simulation on a very large number of cores relative to CPU for an affordable price. The result is a drastic reduction of the computation time (around 100 times). Therefore, the time required to execute a simulation is significantly reduced and larger models such as the one considered for three-dimensional simulations can be realized. All simulations presented in this thesis were conducted using Pogo.

1.2.1 Explicit time domain FE

The elastodynamic equation can be discretized in the spatial domain:

$$M\ddot{u} + C\dot{u} + Ku = F \tag{1.11}$$

where $\ddot{u}$, $\dot{u}$, and u correspond to the acceleration, the velocity and the displacement respectively. M is the diagonal lumped mass matrix whose values are determined by the density of the material. K is the static stiffness matrix whose values are defined by the Young's modulus and Poisson's ratio. C is the viscous damping matrix which is determined by the Rayleigh damping. F is the external force vector. Wave propagation occurs when the initial equilibrium is disturbed by the application of forces or displacement constraints on nodes. Commonly, these are applied in the form of a tone burst.

This equation can be solved by stepping through in time, at each increment calculating the nodal values for the next increment. Details and full equations are outlined in (Huthwaite, 2014). Linear elements are used in order to solve the equations. In elastodynamic materials, each node has 3 degrees of freedom for 3D models and 2 degrees of freedom for 2D models while for fluids (water for example) there will just be pressure, which is a scalar, giving 1 degree of freedom per node. Each node of the mesh is tied to the nodes adjacent.

1.2.2 Absorbing boundaries

The default FE boundary condition is a free boundary, i.e. sound soft. This corresponds to being connected to a medium with a very low acoustic impedance, such as a vibrating object in a vacuum. However, in many cases, models have a large or infinite domain. In order to avoid interferences of boundary reflections with the area of interest, the FE models used in this thesis use absorbing boundaries that absorbs all outgoing waves completely, around the region of interest, and truncate the domain at this location. Doing so is highly challenging, and is still the subject of active research across a number of wave modalities. In this thesis, the preferred approach is an absorbing region, where the damping gradually increases as the wave propagates into the medium. This gradual change minimises the acoustic impedance mismatch, so helps to minimise any reflections from the boundary. The thickness of these absorbing boundaries has to be at least 3 to 5 wavelength in order to work properly (Rajagopal, Drozdz, Skelton, Lowe, & Craster, 2012).

1.2.3 Element size and time increment

FE simulations must respect two criteria to reduce errors during calculation: (1) the element size must be much smaller than the wavelength and (2) the step time must be chosen to ensure that the fastest travelling wave packet travels through each layer of elements. Not respecting the criteria leads to either drastic calculation times or incorrect results.

1.2.3.1 Element size

According to previous studies (M. Drozdz, Moreau, Castaings, Lowe, & Cawley, 2006), at least 10-15 elements per wavelength are necessary to ensure convergence of the mesh. The shortest excited wavelength must be considered to determine the element size. Indeed, several modes with different wavelengths can be excited. A ratio of 15 elements per wavelength was used in all simulations presented in this thesis.

1.2.3.2 Time increment

The step time or time increment must be chosen under the time it takes the fastest wave to travel through an element (Cook, Malkus, Plesha, & Witt, 1974). Cook defined the following equation to determine the step time Δt:

$$\Delta t = 0.8 \frac{\Delta x}{V_{ph\_Max}} \tag{1.12}$$

where Δx is the smallest element size, V_{ph_Max} is the fastest phase velocity and 0.8 is a safety factor.

1.2.4 Modelling water as a solid

The software used in this thesis (Pogo) is currently unable to model acoustic elements. However, water was required in Chapter 3. This section details how to approximate water as a viscoelastic fluid which means with the properties of a solid material and using solid elements

(Young's modulus (E), Poisson's ratio (υ), density (ρ) and damping (α)).

1.2.4.1 Determination of parameters

The density of water (ρ=1000 kg/m^3) and the bulk modulus of water (K=2.2 GPa) are well known. The Poisson's ratio and Young's modulus are linked by the relation:

$$E = 3K(1 - 2\nu) \tag{1.13}$$

The speed of sound in water (V_l=1480 m/s) depends, for the solids, on the Young's modulus, the Poisson's ration and the density:

$$V_l = \sqrt{\frac{E(1-\upsilon)}{\rho(1+\upsilon)(1-2\upsilon)}} \tag{1.14}$$

Using equations (1.13) and (1.14) the properties to model water as a viscoelastic fluid can be determined:

- Density: ρ=1000 kg/m^3
- Young's modulus: E=40 MPa
- Poisson's ration: υ=0.497

1.2.4.2 Verification

The major issue in modelling the water as a solid is that shear waves cannot propagate in fluids but can in solids. The amplitude of the shear component G can be determined using:

$$G = \frac{E}{2(1+\upsilon)} \tag{1.15}$$

For υ=0.497, shear waves have an amplitude 15.6 dB lower than longitudinal waves therefore an approximation of no shear component in the water modelled as a solid can be made.

The transmission and reflection coefficients depend on the acoustic impedance of the materials. The acoustic impedance is equal to the product of the bulk velocity and the density of the material. As both parameters are the same for the water modelled as an acoustic element or a solid, the acoustic impedance stays the same. Therefore, the properties of reflection/transmission remain unchanged.

In order to compare both types of elements and properties, two simulations have been carried out. One with Abaqus and the second one with Pogo. The simulation parameters were the same except for the parameters of the water (acoustic elements defined by a bulk modulus for the Abaqus simulation and solid elements with the parameters determined previously for the Pogo simulation). No absorbing boundaries were used. The 2D FE model is composed of a 100 μm thick layer of water and a 100 μm thick layer of steel. The excitation is a 5 cycle tone burst centered at 150 MHz and applied as a force on a single node on the external face of the steel section along the y-axis. The element size selected was 0.6 μm and the time increment 0.1 ns. Figure 1.3 shows both simulations at a certain time step when a part of the signal is transmitted inside the water and the rest is reflected in the steel section. The echoes of the steel section on the Abaqus simulation are not visible due to parameters in the display options. This comparison shows that transmitted signals in both simulations are very similar, confirming the possibility of modelling water with solid elements. However, it is impossible to compare the amplitudes as Abaqus displays a pressure due to acoustic elements and Pogo displays a magnitude of displacements due to the solid elements.

The main issue remaining is to make an excitation inside the water. Indeed, with acoustic elements it is unnecessary to choose a direction of excitation because the pressure is applied in all directions. However, with solid elements it is not possible to do so. Therefore, the force has to be applied in a direction. This issue is not very important in our situation as the excitation will be applied and received outside the water on solid nodes.

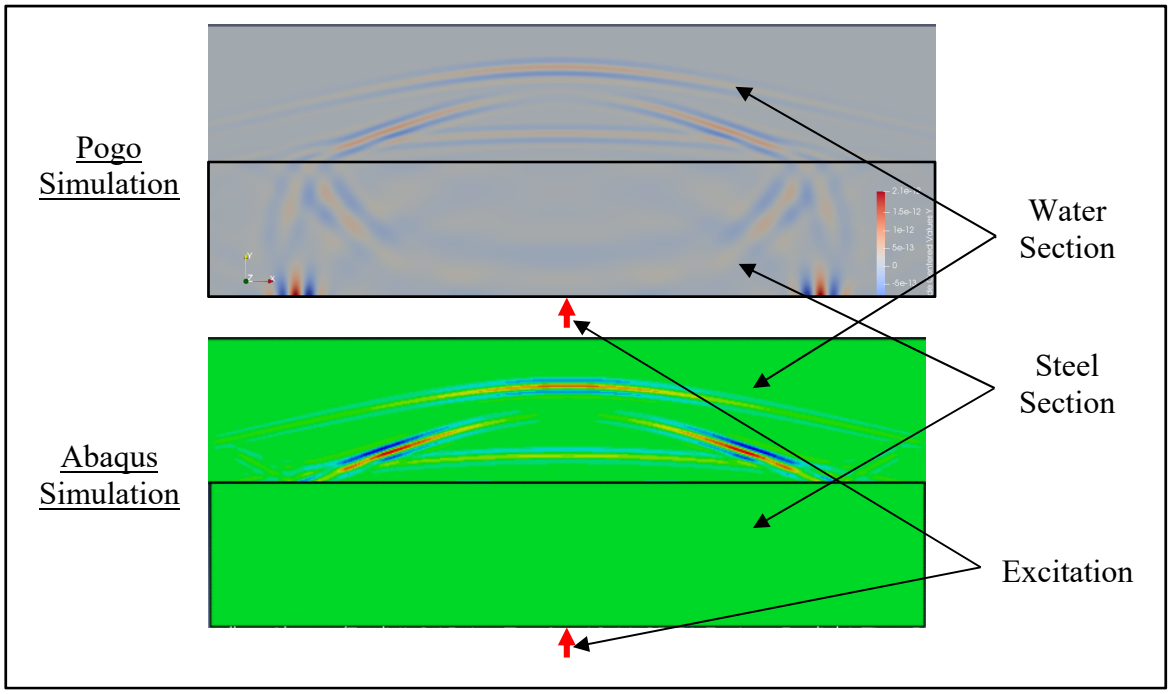

Figure 1.3 Comparisons between Abaqus where the water modelled with acoustic elements and Pogo where the water modelled with solid linar elements

1.3 Laser welds on fuel cell bipolar plates

1.3.1 Fuel cell bipolar plates

A fuel cell comprises an anode, a cathode, and an electrolyte membrane (Blomen & Mugerwa, 2013). It works by circulating hydrogen through the anode and oxygen through the cathode. The hydrogen molecules are split into electrons and protons at the anode site. Then, the protons pass through the electrolyte membrane, while the electrons are forced through a circuit, generating an electric current and excess heat. At the cathode, the protons, electrons, and oxygen combine to produce water molecules. One recent configuration of fuel cell stack uses the proton exchange membrane fuel cells invented at General Electric in the early 1960s (Niedrach, 1964) and improved since (J. Zhang, 2008), which combine the anode and cathode in a single part called a bipolar plate (BiP). Figure 1.4 describes the main components of the stack (Peng, Yi, & Lai, 2014). The BiP (called BPPs in the Figure 1.4) supplies the gases

through the flow channels to the electrodes, provides structural support for the membrane and facilitates water and heat management within the cell.

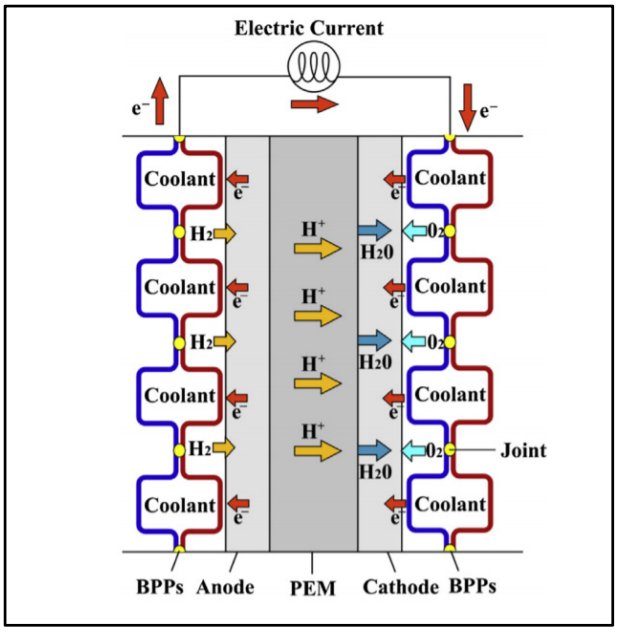

Figure 1.4 Schematic representation of the main fuel cell stack components and BiP functions: structural support, reactant channel, coolant channel, electric conduction and water management (not to scale)

Taken from (Peng, Yi, & Lai, 2014)

The BiP investigated in this thesis are composed of two stainless steel plates with a thickness around 100 µm, joined with laser welds. Figure 1.5 shows the approximate BiP geometry and flow channels of the cathode side. Most of the drawing is hidden for reasons of confidentiality.

The fabrication process of the BiP can be described in four main steps: the forming, the joining, the coating and the assembly. First, stainless steel plates are cut and then stamped so as to create the complex flow channels. Then, the two plates composing the BiP are joined with laser welding before being externally coated to protect the plates from corrosion and improve the electrical conductivity. Finally, the plates are assembled with other components to make a fuel cell stack.

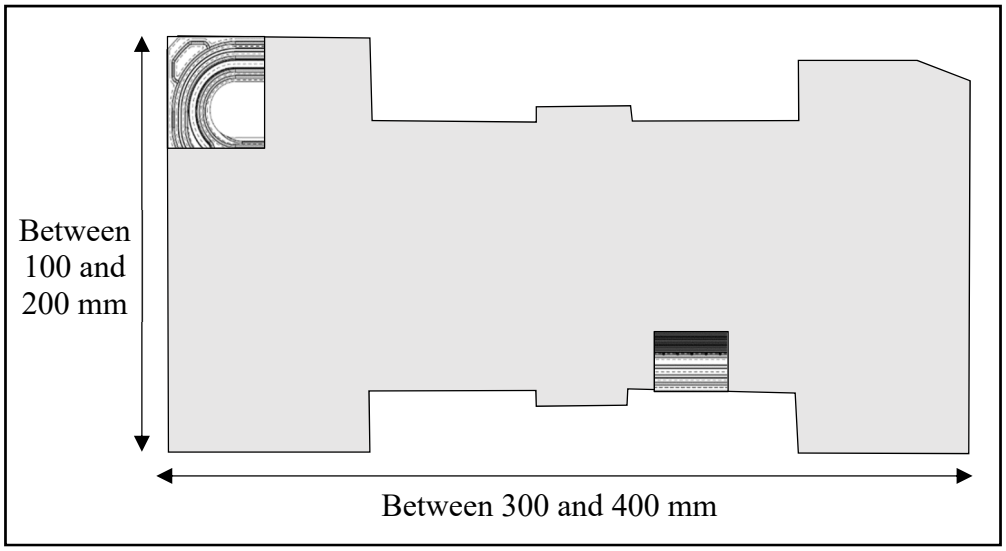

Figure 1.5 Bipolar plate approximate geometry and features. View from the cathode side. The linear and spot welds to be inspected are represented by dotted lines

BiP manufacturing uses two types of laser welds: continuous welds and spot welds. Both could be defective and lead to external leaks. The welding is typically performed from the cathode side. Both types of welds are shown in Figure 1.5 with dotted lines. Linear welds are approximately 200 µm large and have a bump on both sides (around 20 µm on the anode side and 10 µm on the cathode side). Spot welds are about 150 µm in diameter with bumps of a similar the size to the continuous welds. The spots are typically between 200 and 250 µm apart.

As explained in the introduction, one common failure is when the coolant channels of the BiP are pressurized leaks may be observed. Coolant channels are inside the BiP, in between the two plates.

1.3.2 Common laser weld failures

This project aims to find and characterize the causes of the leaks occurring in the BiP. It is important to know the types of defects laser welds can present. There are many kinds of defects that can occur with welding. The main defects are classified in (ISO, 2007), (Katayama, 2013).

Figure 1.6 illustrates the main defects that could happen during the manufacturing process of BiP. Many parameters influence the formation of these defects. Knowledge of which defect causes the leaks will help manufacturers improve the quality of BiP.

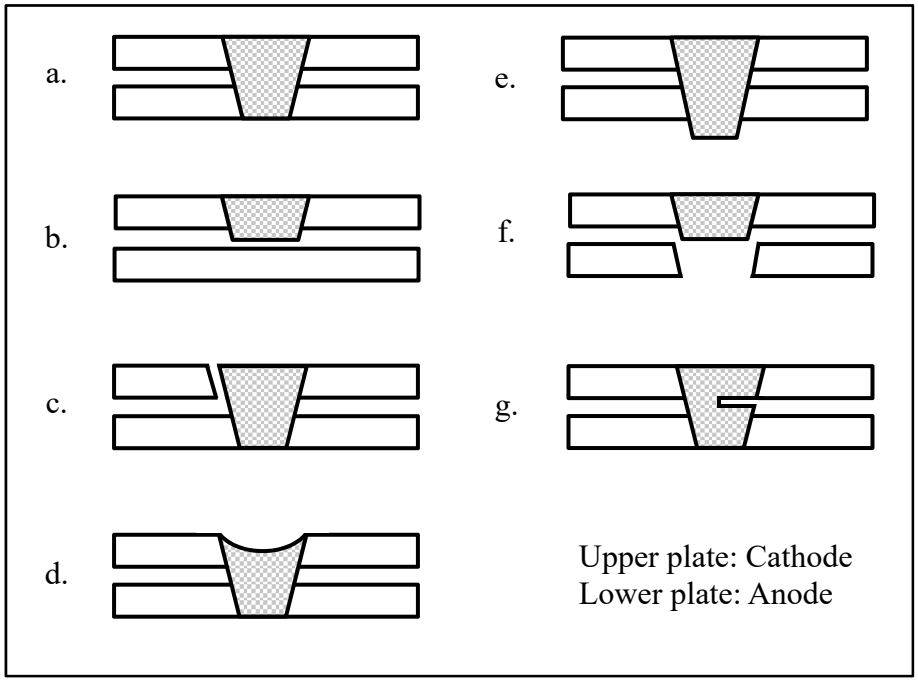

Figure 1.6 Main defects that could happen on BiP welds. The upper plate corresponds to the cathode and the lower to the anode. a. Good weld geometry but with Young's modulus variation. b. Weld not through, c. Diagonal crack, d. Undercut, e. Bumps (can also be on the cathode), f. Hole in the anode (can also be on the cathode), g. Horizontal crack (can also be on the cathode)

1.4 Nondestructive testing methods

No current nondestructive testing methods have the ability to help in identifying defective welds or the cause of leaks. Indeed, the method used at the moment is to clamp the bipolar plate on a setup inside a tank of water. Then air pressure is injected in between the anode and the cathode. If a weld is defective, bubbles leak from the sample. The area is then marked and inspected with a microscope. One idea would be to find where the leak is located and make a cut of the area to be inspected and therefore understand the cause of the leak. But it is practically impossible to determine the precise location of the defective welds as their

dimensions are very small and the microscope is able to determine external defects but does not provide information on internal defects such as delamination or cracks. Therefore, other NDT methods must be investigated.

1.4.1 Conventional nondestructive techniques

The main NDT used on welds to find and characterize defects are the liquid penetrant method, eddy current testing, magnetic particles testing, radiography testing and ultrasonic testing (Ditchburn et al., 1996). All these techniques are used in the industry to find defects in welds. But these conventional techniques are aimed to inspect large welds with dimensions above a few millimeters. Moreover, most of these methods are able to point out a defect but are not able to characterize it. The only NDT that can make an image through the inspected structure are radiography and ultrasonic testing.

Radiography uses a source of X-rays or gamma-rays to radiate the sample to be inspected. The electromagnetic radiation going through the sample is then recorded on a screen making an image of the part. This image is greyscale. It images the density of the sample between the source of the screen. If no material was crossed, the intensity received is maximal and the pixel is black. If no radiation is received, then the density crossed is too important and the pixel becomes white. But industrial radiography is not suitable to the problem of interest in this thesis because the resolution is too big compared to the size of the anticipated defects (the resolution is insufficient). Moreover, only volumetric defects can be detected. Cracks do not change the density of a material even locally, thus cracks would not be detected.

Micro computed tomography (μCT) is an improvement of radiography that captures a series of 2D planar X-ray images by rotating the sample and reconstruct the data into 2D cross-sectional slices. These slices can be further processed into 3D models. The μCT has the advantage to be much more accurate than traditional radiography thanks to multiple images used to reconstruct the model. Therefore, smaller defects can be detected (up to 100 nm). However, only volumetric defects are detected. Moreover, the cost involved due to the size of

BiP and duration of measurement (a few hours) would be very challenging. Therefore, it is not a good solution to the problem of inspection of BiP.

1.4.2 Ultrasonic nondestructive testing

Ultrasonic testing seems to be the best option to characterize defects inside thin welds as ultrasonic NDT is able to detect non-volumetric defects such as cracks. However, conventional ultrasonic testing such as mono-element pulse-echo inspection uses frequencies between 40 kHz and 20 MHz. Even at 20 MHz, the frequency is not high enough as the wavelength in stainless steel would be around 280 μm which is much larger than the thickness of the plates. Therefore, other techniques using ultrasonic waves must be investigated: GW and SAM.

1.4.2.1 Ultrasonic guided waves

In GW testing, acoustic waves are excited by a probe and propagate along the structure guided by its boundaries. GW are mainly used for long-range pipeline or rail inspection (Cawley, Lowe, Alleyne, Pavlakovic, & Wilcox, 2003), but can also be used at higher frequencies to characterize materials (Chimenti, 1997), and for example properties of welds (Arone, Cerniglia, & Nigrelli, 2006; Comot, Bocher, & Belanger, 2017; Dixon, Edwards, & Palmer, 1999). GW can be used with ultrasonic phased arrays in order to image geometries or defects (P. D. Wilcox, 2003; Yan & Rose, 2007).

1.4.2.2 Scanning acoustic microscopy

SAM is similar to a mono-element pulse-echo inspection in immersion but at very high or ultra-high frequency (Briggs, Briggs, & Kolosov, 2010; Maev, 2008). Indeed, a SAM is a pulse-echo (reflection-type) microscope that generates images using a focused acoustic lens at frequencies usually ranging from 10 to 100 MHz. It is composed of four main elements: a transducer, an immersion tank, motorized XYZ stages and the sample requiring inspection. The sample is immersed in the tank as well as the tip of the transducer. Various fluids can be

used has the coupling medium such as water or an inert fluid. Figure 1.7 shows the diagram of an acoustic microscope. The transducer is composed of a piezoelectric transducer and a spherical acoustic lens that focusses the beam. The transducer alternatively acts as a sender and a receiver. The incoming wave enters the sample, and echoes are produced at the sample surface and at specific interfaces within the sample. Motorized stages move the transducer above the sample and the position is measured. The focal point is typically inside the sample but is shortened considerably because of refraction at the liquid-solid interface. The angle of the rays from the lens is kept small to avoid total reflection between the coupling fluid and the sample.

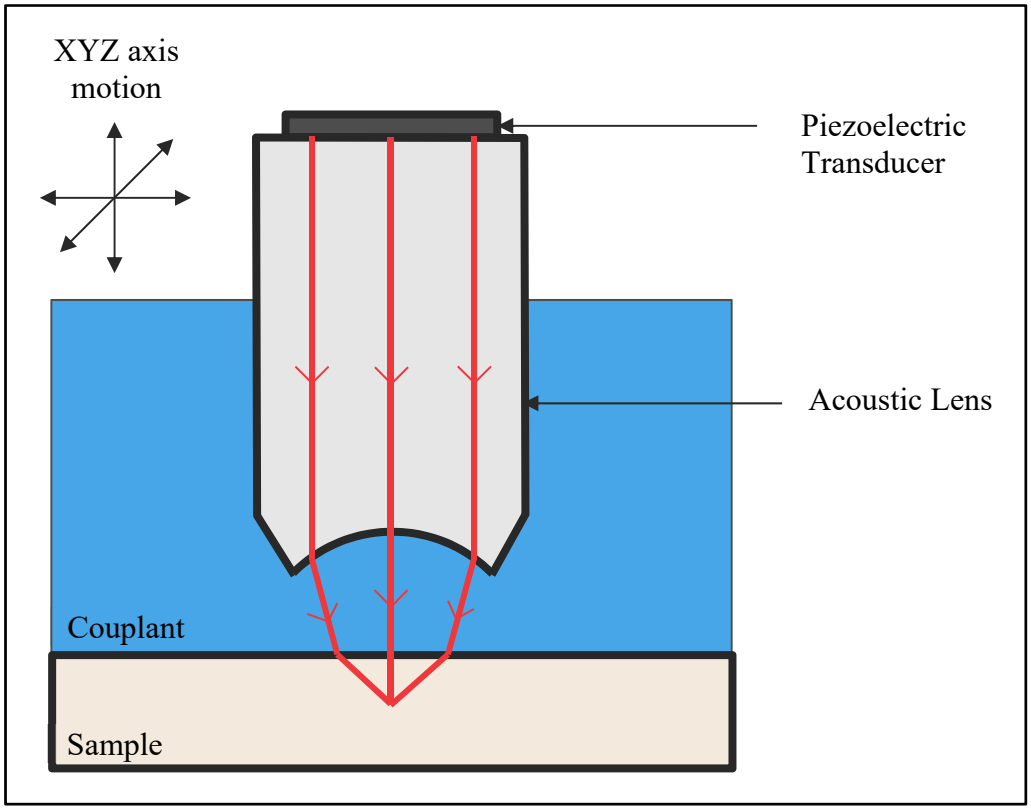

Figure 1.7 Main components in a SAM: Piezoelectric transducer mounted on an acoustic lens. The acoustic beam is represented by the red lines. This beam is focused inside the sample and the back propagating echoes are recorded by the same transducer

1.4.3 Ultrasonic imaging techniques

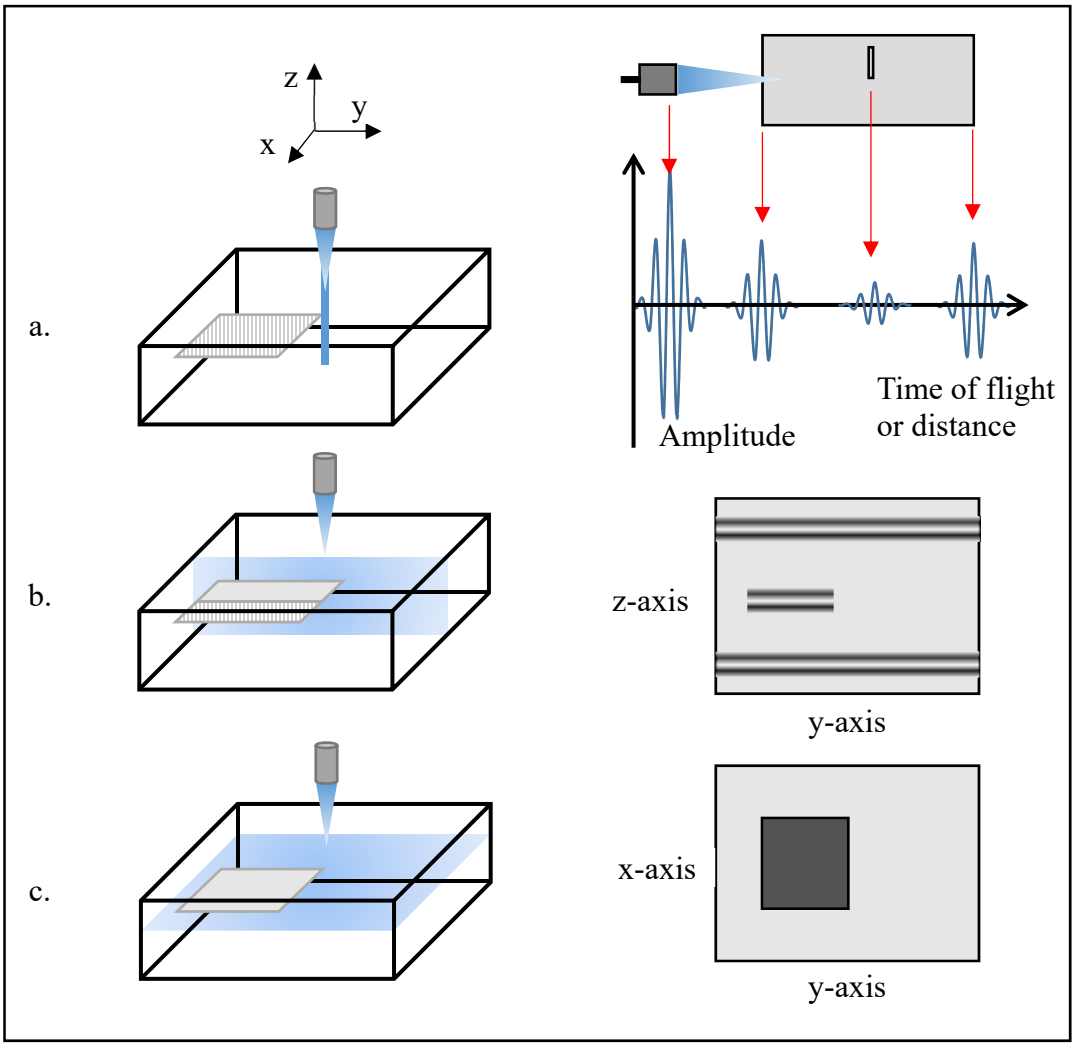

Figure 1.8 Fundamental methods for presenting the data of conventional ultrasound. a. A-Scan, b. B-Scan, c. C-Scan

1.4.3.1 A-Scan

An A-Scan is an oscilloscope display of the echo pattern (Mountford & Wells, 1972). The received pulse amplitude is represented as an amplitude along the time axis, as illustrated in Figure 1.8 a. The grey cylinder represents the transducer and the grey rectangle represents the sample with a notch in the middle. A-Scans are useful to show the amplitude level and the

time-distance relationships of the features inside samples from the surface. They are the easiest way to display raw data. At each position, a SAM acquires an A-Scan.

1.4.3.2 B-Scan

B-Scans are a combination of A-Scans with the position of the probe along the surface (Fatemi & Kak, 1980). The transducer scans along a lines in x or y direction. It depicts the acoustical side projection of the object. The amplitudes are typically represented on a color scale. The depth of different structures within the sample can be measured. Figure 1.8 b. illustrates a B-Scan image. The upper lines are the first received signals corresponding to the surface of the sample. The lines at the bottom correspond to the backwall of the sample. The lines in the middle are due to the defect in the middle of the sample.

1.4.3.3 C-Scan

C-Scans is an imaging technique that uses the data of both scanning directions (x and y). On the received signals, a gate is selected around a zone of interest, generally around the depth of the defect with a width of the length of the signal. The maximum amplitude received inside this gate gives the color of the pixel. Figure 1.8 c. illustrates C-Scan.

1.4.3.4 Others

There are many other imaging techniques can be used to improve the resolution or reduce artefacts. The three techniques presented previously are the most commonly used. This thesis also investigated other imaging techniques such as Synthetic Aperture Focusing Technique (SAFT) (Doctor, Hall, & Reid, 1986; Trots, Nowicki, & Lewandowski, 2009), Total Focusing Technique (TFM) (C Holmes, Drinkwater, & Wilcox, 2004; Caroline Holmes, Drinkwater, & Wilcox, 2005; Long, Russell, & Cawley, 2012), or ultrafast plane wave imaging (Tanter & Fink, 2014; Tiran et al., 2015). The theory of these techniques was omitted, as it is not fundamental in the comprehension of the thesis.

CHAPTER 2

INSPECTION USING ULTRASONIC GUIDED WAVES

One of the solutions that was investigated to characterize defects in thin laser welds was the use ultrasonic GW. Ultrasonic GW has already been used to characterize some properties of linear welds (Arone et al., 2006; Comot et al., 2017; Dixon et al., 1999; Yu, Zuo, Xiao, & Fan, 2019) and spot welds (Zhenhua, Shi, & Zhao, 2008). However, the ultrasonic GW methods were developed for much bigger welds. Therefore, the aim of this chapter is to assess the feasibility of inspection in thin stainless steel plates.

2.1 Inspection methods

The sample comprises two stainless steel plates welded together. For the simulations, the thickness of the plates was considered to be 100 µm and the width of the weld to be 250 µm in this case. Each plate was assumed to behave like a free waveguide. In the inspection scenario schematized in Figures 2.1 and 2.2, GW would be excited on one of the plates in the vicinity

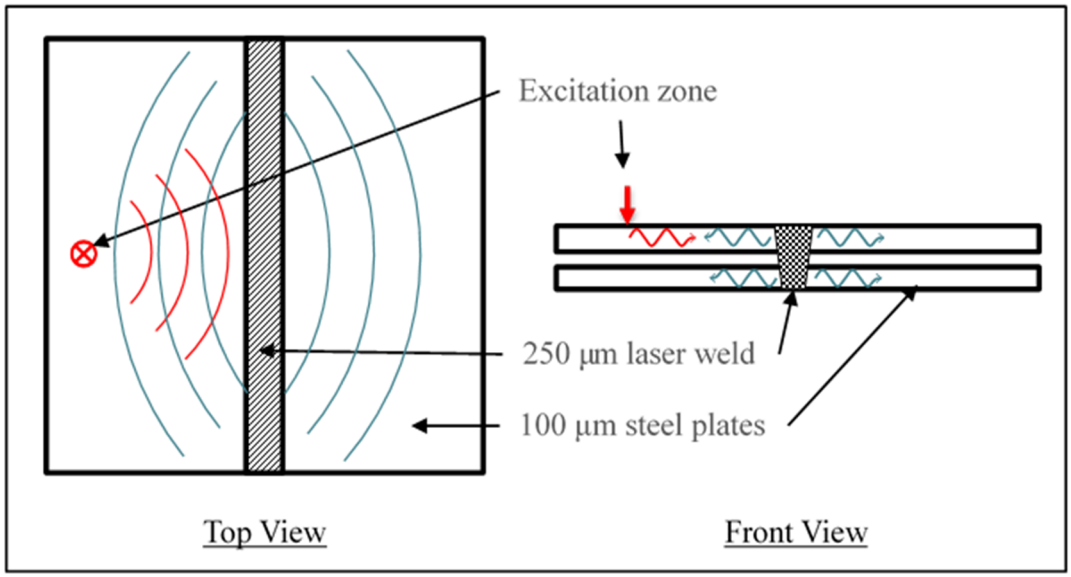

Figure 2.1 Illustration of the GW inspection method. The red lines corresponds to the excited wave packet that propagates inside the plate towards the weld line and the blue lines are the result of reflection from the weld and transmission through the weld

of the weld line. GW would propagate inside the plate up to the weld line where they would interact with the weld. The energy would then split in all possible directions.

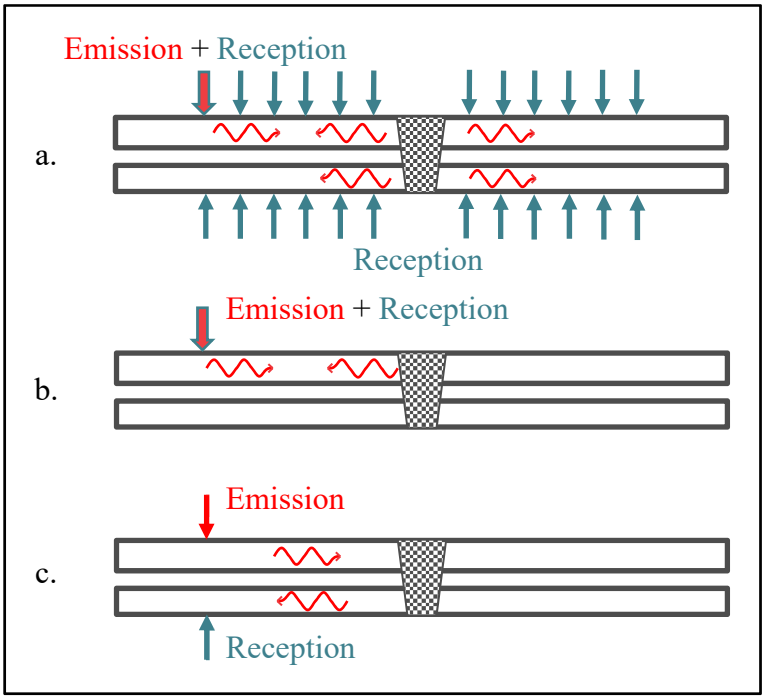

Figure 2.2 Schematic of the possible configurations. a. spatial energy distribution. b. Pulse-echo method. c. Pitch-catch method

Using the energy transmitted through the weld, three configurations would then be possible as shown in Figure 2.2:

- The spatial energy distribution method is illustrated in Figure 2.2 a. Measurement points are located along the four possible branches. Multiple measurement points distributed spatially allow the calculation of two-dimensional Fourier transforms (FFT 2-D) (Alleyne & Cawley, 1991) of the monitored signals along each branch. Therefore, the energy of modes propagating in each branch can be calculated. The idea is to understand whether there is a link between the energies and the weld properties (width, gap, Young's modulus).

- The pulse-echo method is illustrated in Figure 2.2 b. The back-scattered signals are recorded at the same location as the excitation. This method could be used with a phased array probe (with the elements parallel to the weld) in order to make an image of the weld geometry. This method can also be adapted for measurements in transmission such as in Figure 2.2 c.

In order to reduce the complexity of the signal post processing, the frequency of excitation must be chosen to be under the first cutoff frequency of the waveguide. Figure 2.3 shows dispersion curves in a 100 μm stainless steel plate. The cutoff frequency of the first high order mode is around 25 MHz. At a frequency of 10 MHz, only the two fundamental Lamb wave modes can propagate (A_0 and S_0). The two modes have a significant difference in phase velocity. The phase velocity of S_0 is approximately twice the phase velocity of A_0. Moreover, the out-of-plane excitability of A_0 under the cutoff of the first high order mode is much higher than S_0 (P. Wilcox, Evans, Diligent, Lowe, & Cawley, 2002). Therefore, in this frequency range, the differences in the speed of sound and in excitability would make the time domain separation of the modes possible. A 5-cycle Hann windowed toneburst was chosen as a compromise between the spatial resolution and the frequency bandwidth. As the modes are dispersive wide bandwidth signals cannot be used.

The feasibility of these methods was evaluated using FE simulations.

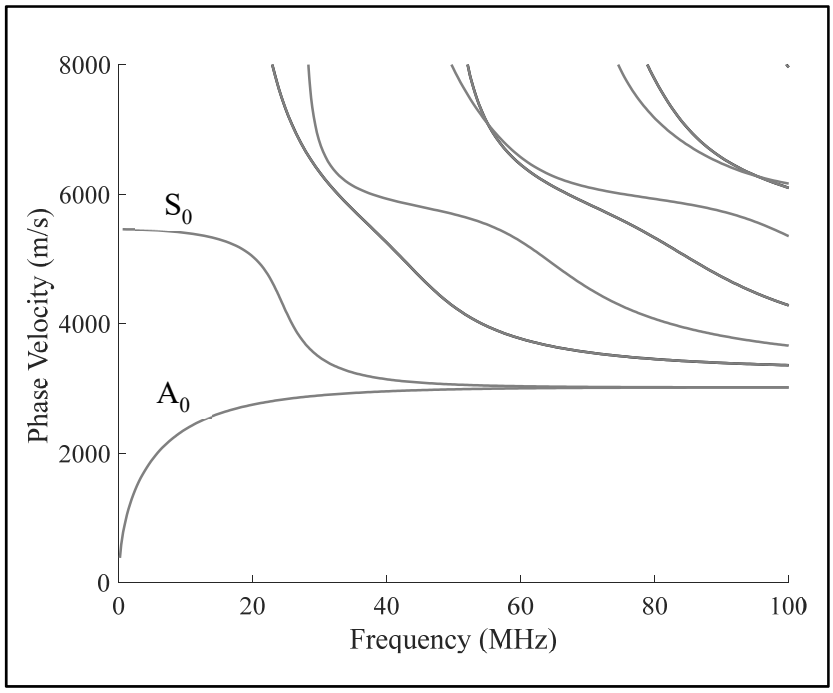

Figure 2.3 Dispersion curves in a 100 μm thick stainless steel plate (E=216 GPa, ν=0.29, ρ=7932 kg/m3)

2.2 Finite element simulations

This section details the models and parameters used for each method of inspection.

2.2.1 Models

2-D and 3-D models were used depending on the method of inspection. The spatial energy distribution method illustrated in figure 2.2 a., was modelled with a 2-D FE model as the purpose of this simulation was to characterize whether there is any difference in the modes energy distribution as the weld characteristics change. This problem is symmetrical (along the out of plane axis) and a 2-D model was deemed sufficient. The model geometry is shown in Figure 2.4.

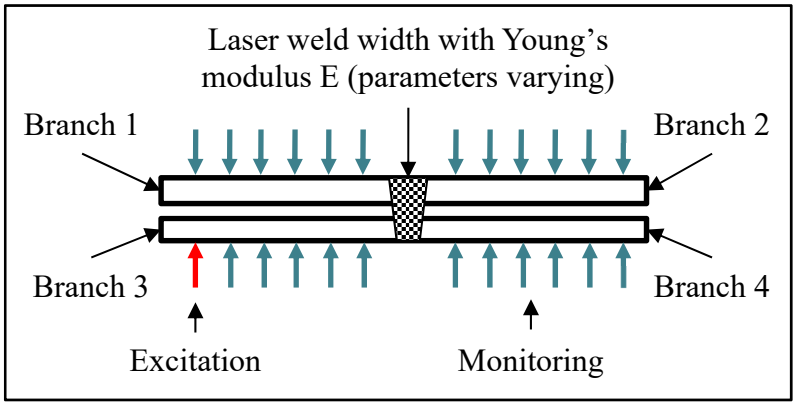

Figure 2.4 Geometry of the 2-D FE model for the spatial energy distribution method

The pulse-echo and pitch-catch modes, illustrated in Figure 2.2 (b. and c.), were modelled with a 3-D FE model as the purpose is to image the weld geometry using a phased array probe. Therefore, the third dimension was required. The 3-D model geometry is shown in Figure 2.5.

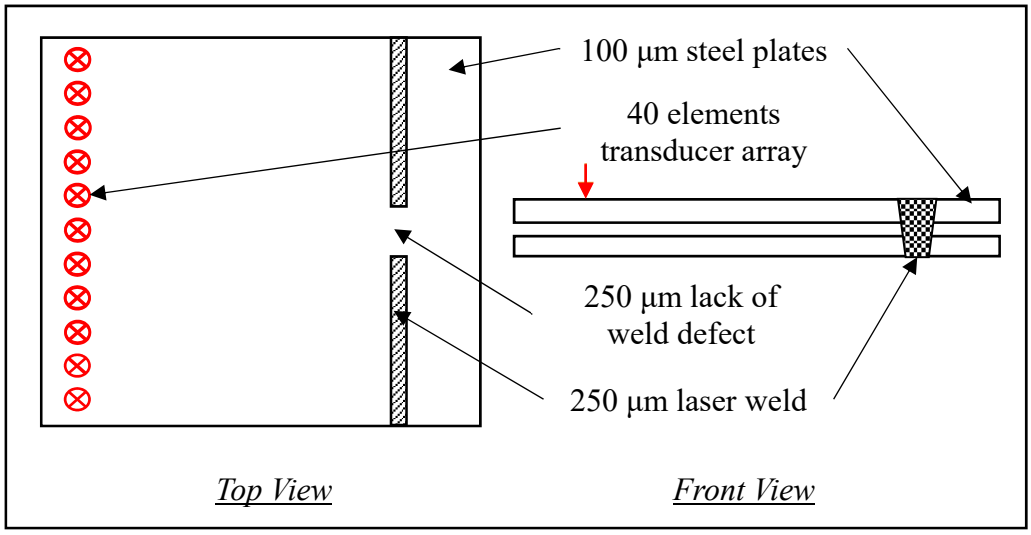

Figure 2.5 Geometry of the 3-D FE model for the pulse-echo methods

Absorbing boundaries on the end of each branch to avoid reflections from the borders and model a weld far from any feature.

2.2.2 Parameters

As explained in the literature review chapter, FE simulations must obey the criteria of element size and step time. Therefore, a minimum of 10-15 elements per wavelength is necessary to obtain an acceptable error on the wave propagation. The element size selected was 35 μm as the smallest wavelength of the model is inside stainless steel (560 μm at 10 MHz). The time increment was chosen using equation 1.12: Δt=5 ns.

All parameters used in the simulation in this chapter are detailed in the Table 2.1;

Table 2.1 Parameters of simulation

Parameter	**Value**
Element Type	- CPE4R (4-noded quadrilateral elements) for 2D simulations - C3D8R (8-noded brick element) for 3D simulations
Excitation Type	Force applied on a single node perpendicularly to the surface (and parallel to the surface for shear horizontal methods)
Excitation Parameters	5 cycle Hann windowed at 10 MHz
Monitoring	Displacement monitored on a single node perpendicularly to the surface (and parallel to the surface for shear horizontal methods)
Time Increment: Δt	5 ns
Element Size: dx	35 μm
Material Properties	Stainless steel: E=216 GPa, ν=0.29, ρ=7932 kg/m3

2.2.3 Hypotheses and consequences

These FE simulations assume some hypotheses:

- The material is assumed to be isotropic and without any attenuation. However, the properties of the plate and the weld are very likely different. The simulations with the

varying Young's modulus in the weld are also aimed to evaluate the consequences of this assumption.

- The modelled geometry is simplified, the plates are perfectly separated, the welds are assumed to be far from any feature, flat and always at the same distance from the excitation. This could cause different results in experimental measurements especially for the variation of the width of the weld or the pulse echo imaging. However, the simulation geometry is sufficient to prove the feasibility of the methods.
- The excitation and monitoring are realized on single nodes normal to the surface. In practice the excitation and monitoring would be on larger surfaces. Modelling these surfaces as singular points improve the resolution of the results.

These hypotheses are intended to reduce the calculation time and simplify the model. However, the simplifications do not reduce the purpose of the simulations, which is to assess the feasibility of the methods of inspection.

2.3 Results

2.3.1 Spatial energy distribution method

The purpose of the spatial energy distribution method is to determine how the energy is distributed along each branches when the Young's modulus or the width of the weld varies. The excitation is performed on the 3rd branch (see figure 2.4). All 4 branches are monitored in order to compute the energy of the propagating modes using the 2D-FFT. The 2-D FE model was detailed in Figure 2.4. The space between each monitoring point was 100 μm and the distance from the excitation point to the weld was 3 mm corresponding to approximately 14 A_0 wavelengths. Two different parameters were investigated: varying the Young's modulus and varying the width of the weld.

2.3.1.1 Variation of the width of the weld

Figure 2.6 shows the 2-D FFT on each branch with a weld width of 200 µm. A_0 and S_0 are clearly identifiable and the energies are normalized to the maximum amplitude of the four branches. Therefore, the maximum amplitude of each branch can be determined.

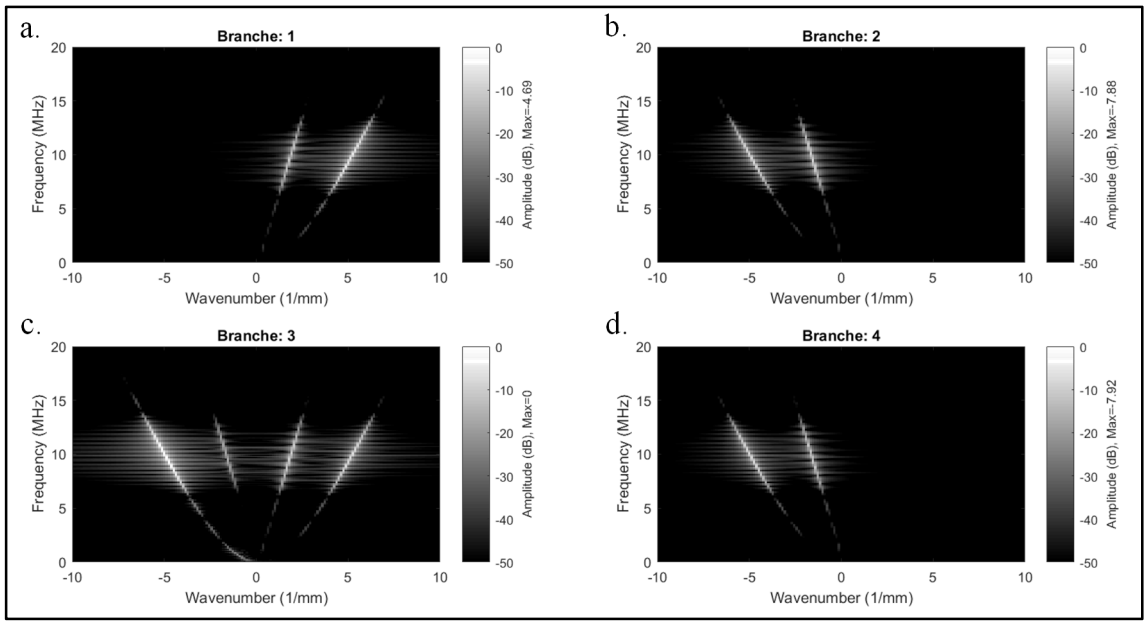

Figure 2.6 2-D FFT on each branch: spatial energy distribution of modes

Figure 2.7 shows the maximum amplitude of each FFT 2-D as a function of the width of the weld. The step size of the weld width was 10 µm between 0 and 100 µm and then was 100 µm between 100 and 2000 µm. The relative amplitude of each branch is relatively constant. There is not a clear pattern of the energy distribution depending on the width of the weld. Therefore, this method cannot be used to determine the width of the weld.

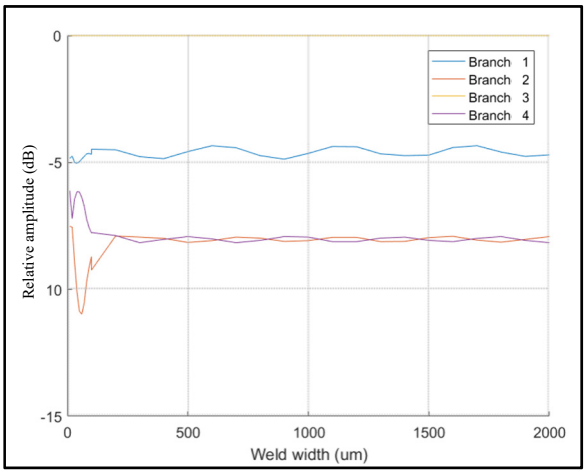

Figure 2.8 Maximum amplitude of each FFT 2-D depending on the width of the weld for a Lamb wave excitation

The simulations were repeated with shear horizontal waves with similar results (Figure 2.8). The results are the same, the relative amplitude does not depend on the weld width. The energy distribution of the fundamental ultrasonic guided wave modes in the four branches can therefore not be used to size the weld width.

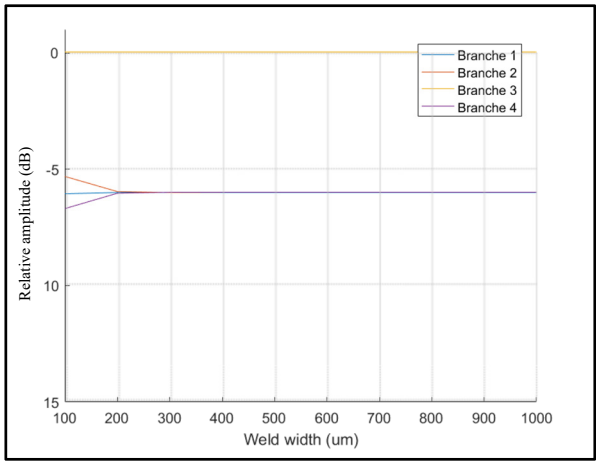

Figure 2.7 Maximum amplitude of each FFT 2-D depending on the width of the weld for a shear horizontal wave excitation

2.3.1.2 Variation of the Young's modulus of the weld

A similar set of simulations were run with a 200 µm weld but this time the Young's modulus was varied. The results are shown in Figure 2.9. Once again, variations in the amplitudes along each branch were too small to be used as a means to determine the Young's modulus of the weld.

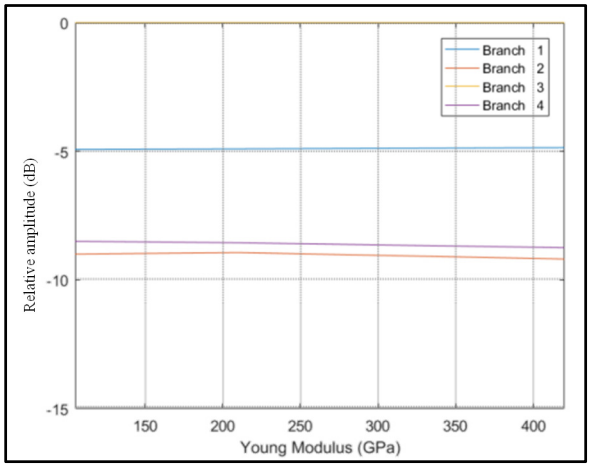

Figure 2.9 Maximum amplitude of each FFT 2-D depending on the Young's modulus of the weld for an out of plane excitation (Lamb waves)

2.3.1.3 Conclusion

Even though this method would enable the detection of a lack of weld when the plates are not mechanically attached, it was rejected based on the fact that variations of the geometry or the material properties inside the weld line could not be detected.

2.3.2 Pulse-echo method

The purpose of the pulse-echo method is to image the geometry of the weld by the use of an ultrasonic phased array probe. To do so, 40 elements located at 3 mm from the weld emit and receive the signals back scattered by the weld line. Therefore, an image of the weld can be

formed using the back scattered signals. The 3-D model was detailed in Figure 2.5. The elementary pitch (space between each element) was initially set to 100 µm. The aperture of the transducer was therefore 4 mm and the passive aperture was 1 mm which corresponds to common phased array probe dimensions.

2.3.2.1 Wave propagation

The wave propagation for the excitation of one element is shown in Figure 2.10. The back-scattered signals are received on all elements as in a full matrix capture (C Holmes et al., 2004) (FMC) scenario. Using this 40x40 matrix, imaging algorithms can be compared.

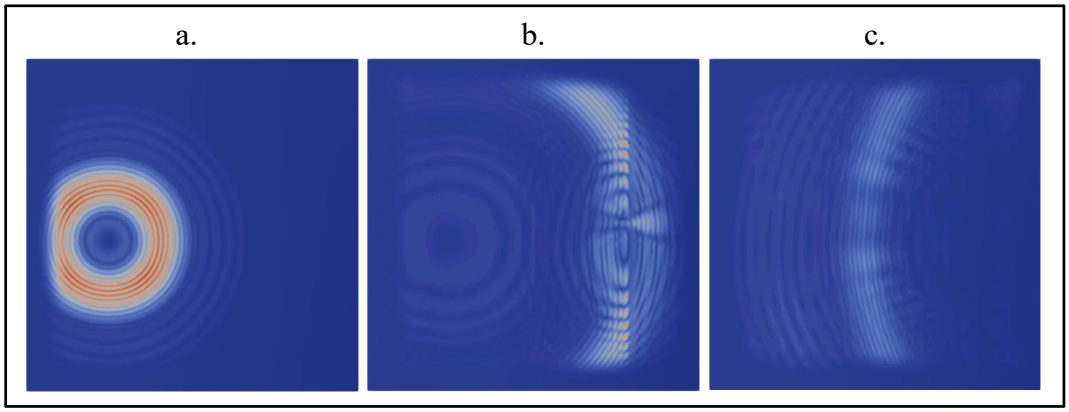

Figure 2.10 Wave propagation for the excitation of a single element on a 6x6 mm^2 plate. a. Excitation. b. Interaction with the weld and the defect. c. Reflection

2.3.2.2 Imaging techniques and results

The FMC acquisition scheme acquires all possible pairs of wave transmission and reception. Using the data, several imaging techniques can be compared. Figure 2.11 shows four different images obtained using different imaging techniques. Each technique has advantages and disadvantages.

Figure 2.11 a. shows a B-Scan. The B-Scan corresponds to a stack of enveloped time traces. It is the simplest and fastest imaging technique. However, it is not possible to identify the lack

of weld. The SAFT is shown in Figure 2.11 b. It is a summation of the pulse-echo signals of each element. The weld is much better imaged and the 250 µm defect is clearly identifiable. Figure 2.11 c. shows the result of the TFM which is the most advanced imaging algorithm that is similar to the SAFT but more complete as all the data of the FMC are used. The defect is well identifiable but the weld is highly attenuated on the sides of the image due to the reconstruction technique. Figure 2.11 d. is the image obtained using the plane wave imaging method. The excitation of this method is different from the previous ones: all elements are excited at the same time making a planar wavefront. The image is the summation of responses to plane waves oriented at multiple angles. The acquisition is much faster and the image of the weld is similar to SAFT.

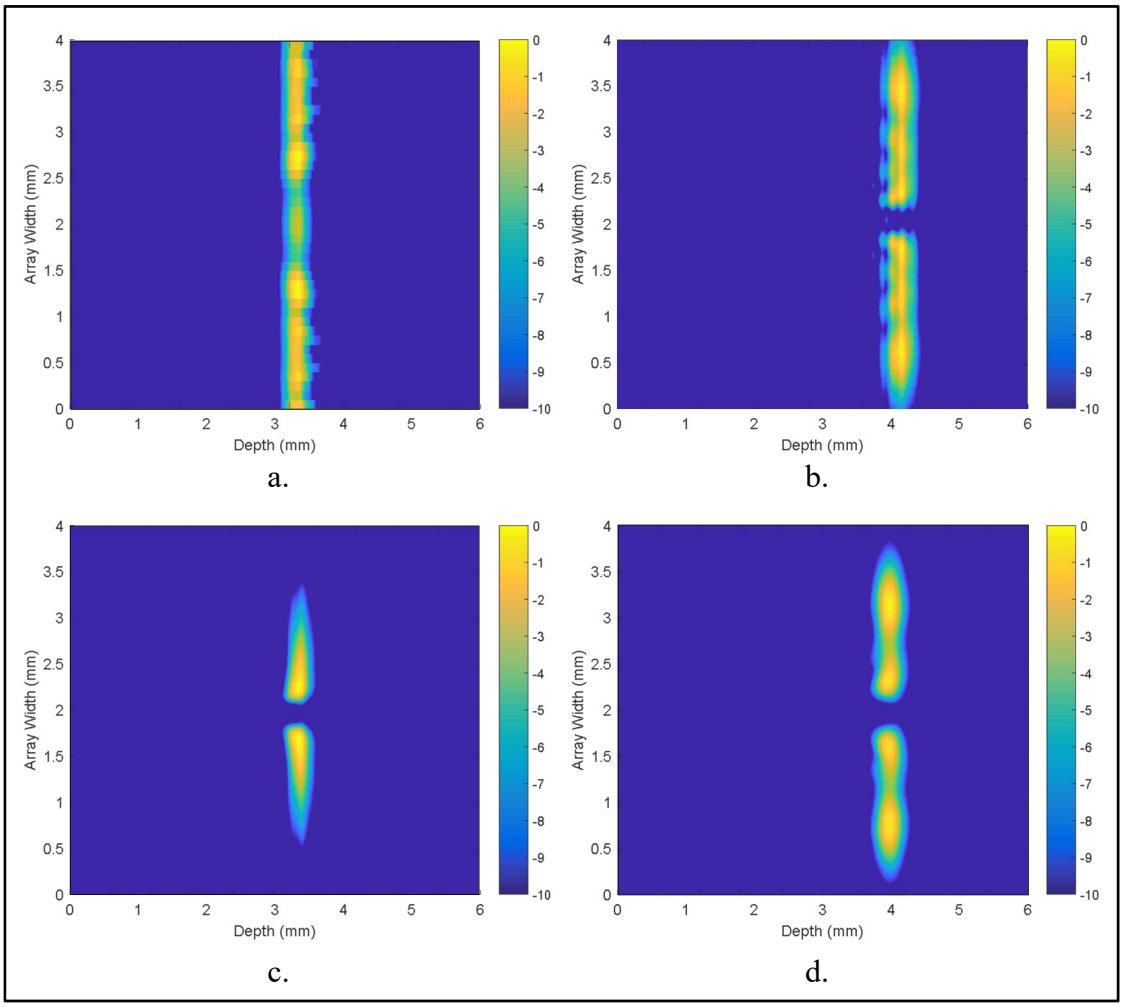

Figure 2.11 Images obtained with four different imaging techniques. a. B-Scan. b. SAFT. c. TFM. d. Plane wave

2.3.2.3 Limitations

The pulse-echo inspection method seems promising as it is able to image the weld geometry. However, this inspection technique is limited to the detection of lack of weld. There is no possibility to detect defects inside the weld such as cracks, lack of penetration or porosity. Moreover, only linear welds can be imaged. Figure 2.12 shows a SAFT image of spot welds. In this case, the distance between the spots was 500 µm. Under this value, the spots cannot be resolved. However, spot welds on the bipolar plates are quite common and usually much closer together.

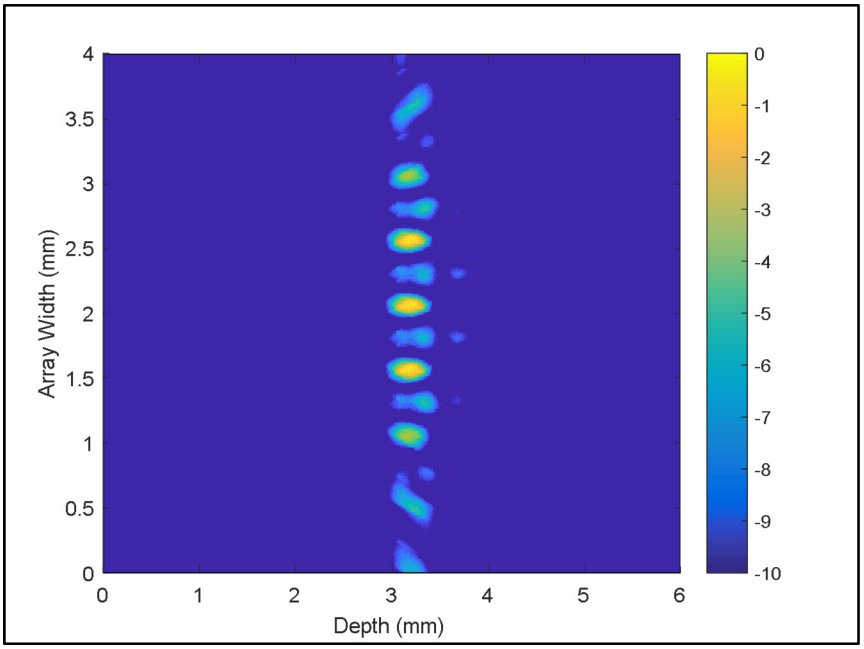

Figure 2.12 SAFT image of spot welds

Moreover, when the geometry of the weld becomes complex such as in the case of curved line weld or the space available between the welds and the features is small the implementation of this method would become difficult.

2.4 Conclusion

This chapter presented various techniques of inspection using ultrasonic guided waves to characterize defects in thin laser welds. These studies were realized with FE simulations. The spatial energy distribution method showed no correlation between the width or Young's modulus of the weld and the energy travelling along the branches. The pulse-echo method was more interesting as an image of the weld could be formed. It is therefore possible to detect a lack of weld in a line weld. However, this method would be limited to this specific application and would only work on continuous line welds. Moreover, the geometry of the welds or the bipolar plates would make this method difficult to implement in an industrial setting.

CHAPTER 3

INSPECTION USING SCANNING ACOUSTIC MICROSCOPY

The second part of this study focuses on the scanning acoustic microscopy (SAM) solution. This technology uses high frequency focused ultrasonic waves to investigate, measure, or image an object. Most applications of SAM is in the semiconductor industry as SAM are able to detect voids, cracks or delamination within microelectronic packages. It is also used in biomedical research to characterize the mechanical properties of tissues. However, the use of SAM in the inspection of defects inside very thin stainless steel laser welds has never been investigated. Therefore, the aim of this chapter is to study the feasibility of that kind of inspection.

3.1 Inspection methodology

3.1.1 Inspection methods

The sample comprised two stainless-steel plates laser welded with a thickness around 100 μm. The overall thickness at the weld is about 200 μm. In SAM, the sample is typically immersed in a couplant (fluid). Thanks to motorized stages, the transducer can pulse and record echoes over the entire surface of the sample. Figure 3.1 shows the reflections occurring after the emission of the signal. In the inspection of interest in this chapter, the first reflection occurs on the top of the cathode, then if the transducer is not above a weld, a second reflection occurs from the cathode backwall. However, if the transducer is above the weld, the second reflection occurs later at the interaction with the anode backwall. Therefore, by scanning with the transducer it is possible to differentiate the welds from the rest as the second echo occurs later. If there is a defect inside the weld, an unusual echo would occur.

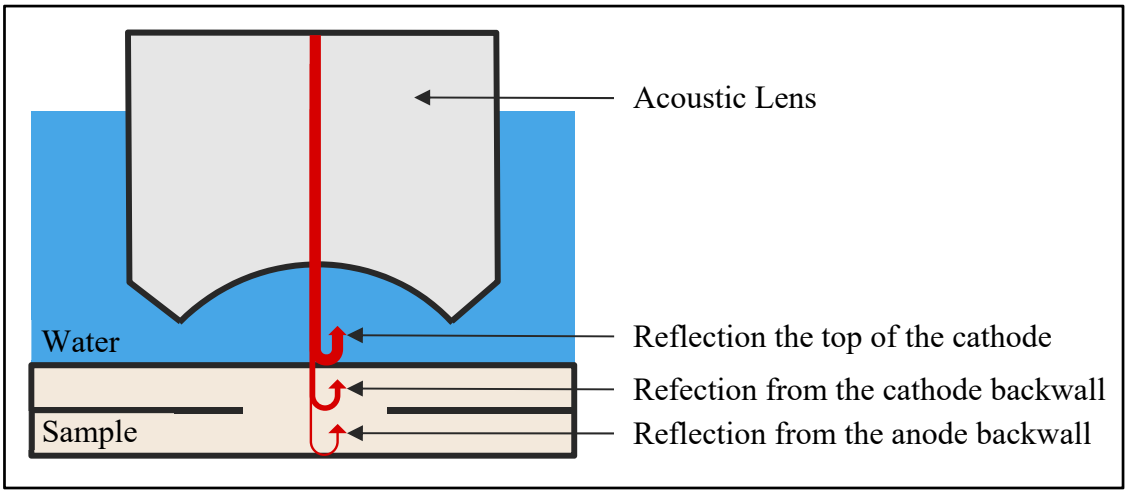

Figure 3.1 Reflections occurring after the emission of the signal with a SAM when located above a weld

3.1.2 Inspection parameters

In order to optimize the image resolution, many parameters have to be carefully chosen. The following section describes the chosen ones.

3.1.2.1 Frequency

Frequency is the most important parameter as the resolution and the attenuation depend on it. The higher the frequency is, the higher the resolution is, but also higher will be the attenuation. The frequencies generally used to detect subsurface damage in microelectronic chips are between 10 and 100 MHz. However, a frequency of 100 MHz leads to a wavelength of 56 µm in stainless steel. As the desired resolution of inspection is around 1/5 of the thickness of the plates, a wavelength of 56 µm would be too large. Therefore, a centre frequency of 230 MHz was chosen as this frequency is available in commercial SAM transducers. However, it was impossible quantify the attenuation in the materials at these frequencies, only experimental test could measure this.

3.1.2.2 Acoustic transducer

The heart of the microscope transducer is the cavity of the acoustic lens and more specifically the aperture and diameter of the cavity. It determines the focal distance of the transducer and influences the resolution. For subsurface imaging, the aim is to maximize the energy that penetrates into the sample. Therefore, it is preferable to use a narrow beam (around 30° aperture lens) in order to reduce the formation of Raleigh waves on the surface and the spherical aberrations due to refraction. Moreover, to reduce the attenuation in the couplant, smaller diameters are preferable as the transducer can be located closer to the sample. Several transducer configurations were tried during the project, each had advantages and disadvantages.

3.1.2.3 Couplant

The couplant is the fluid located between the transducer and the sample. Most of the time, the sample is immersed in this fluid. For the vast majority of applications, water is the simplest option. Indeed, water has relatively low attenuation and is convenient. However, it is not the most effective liquid as other liquids with a more appropriate acoustic impedance and lower attenuation exist. In order to increase the resolution, liquid metal gallium and mercury can be used. Hot water (above 60°C) can also significantly improve the resolution. Finally, cryogenic liquids or high pressure gases such as argon reduce the attenuation but also the acoustic impedance which reduce the energy going inside the sample due to the poor acoustic impedance matching. For simplicity's sake, water at room temperature was used as couplant.

3.2 Finite element simulations

Simulations of SAM have already been performed but remain a challenge due to the very high frequencies. Indeed, high frequencies imply lower wavelengths and thus, lower element size. Therefore the number of elements required increases which the calculation time. Most of previous studies focused on the shape of the acoustic beam produced by the transducer lens

(Che, Guduru, Nurmikko, & Maris, 2015; Tommiska et al., 2018). However, some managed to make simulations of the entire geometry, i.e. having the transducer, couplant and sample in a single simulation (Grünwald et al., 2017).

In this thesis, the aim was also to make a single simulation with all elements in order to have the most realistic and accurate simulations of the welds internal geometry. FE simulations of SAM were conducted using Pogo in order to run the simulations as fast as possible.

3.2.1 Model

Because of the high frequency and the large size of the model, 3-D FE models cannot be simulated on our computer as the number of elements would be too important. Therefore, 2-D FE simulations were used as the problem can be represented in a 2-D plane: see Figure 3.2.

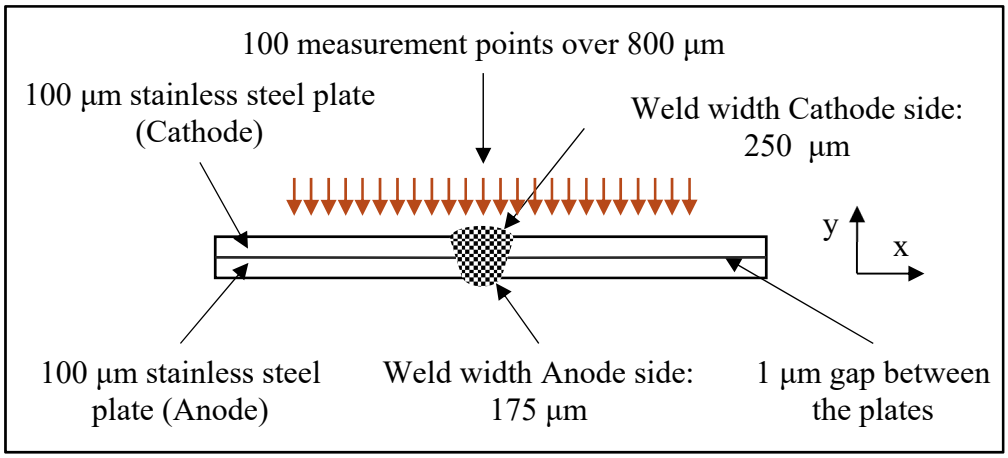

Figure 3.2 2-D FE model geometric parameters of the SAM simulations

Figure 3.3 shows the model used. It is composed of three materials: stainless steel for the sample, water as couplant and sapphire for the acoustic lens. The excitation and monitoring are performed along the y-axis on the nodes inside the lens. For the reception, all the nodes included in the red line are added together in order to get a single A-Scan. Absorbing boundaries surround the lens and the water to avoid reflections.

Figure 3.3 shows the model of the simulation when the transducer is located above the weld. 200 simulations are performed with the weld moving along the x-axis with 4 µm steps. Therefore, a B-Scan combining the 200 A-Scans recorded was used to image the geometry. Moving the weld is equivalent to moving the transducer but it is easier to model.

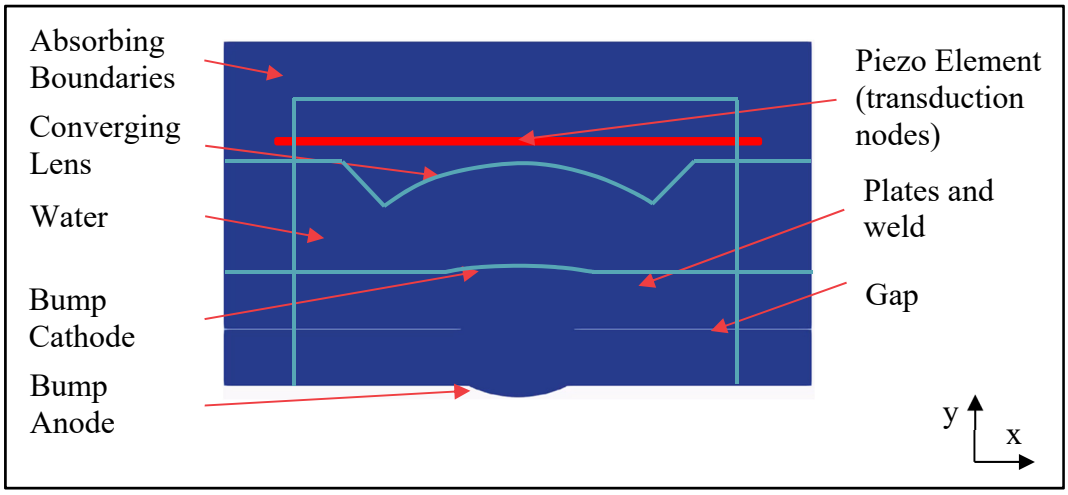

Figure 3.3 2-D FE model of the SAM simulations

3.2.2 Parameters

All parameters used in the simulation in this chapter are detailed in the Table 3.1:

Table 3.1 Parameters of simulation

Parameter	Value
Simulation Type	2D (2 degrees of freedom per node)
Element Type	CPE4R (4-noded quadrilateral elements)
Excitation Type	Force applied on a line of nodes along the y-axis
Excitation Parameters	5 cycle Hann windowed at 230 MHz
Monitoring	Sum of displacement monitored on a line of nodes along the y-axis
Time Increment: Δt	$2.6 \cdot 10^{-11}$ s
Element Size: dx	0.4 µm

Material Properties	Stainless steel (sample): E=216 GPa, ν=0.29, ρ=7932 kg/m^3 Water: E=40 MPa, ν=0.497, ρ=1000 kg/m^3 Sapphire (Converging lens): E=895 GPa, υ=0.29, ρ=3990 kg/m^3

3.2.3 Hypotheses and consequences

The second chapter concerning the FE models of GW inspection methods showed various hypotheses. This chapter contains similar hypotheses:

- Materials are assumed to be isotropic and without any attenuation even inside the weld. A variation of material properties could change the speed of sound inside the weld and modify the final image reconstruction. Moreover, as attenuation is not modelled, the experimental results are expected to have lower intensity especially for double reflections.
- The water was modelled with solid elements. The implications of this assumption were discussed in Chapter 1.
- The modelled sample is simplified (round shapes), the plates are perfectly separated, the welds are assumed to be far from any feature, and symmetric along the out of plane axis. In practice, the welds are not as linear creating many reflections from the surface of the sample.
- The modelled acoustic lens is simplified, as it is symmetric along the out of plane axis. However, an acoustic lens is semi-spherical. The model could not be axisymmetric as the weld is not. The experimental results are expected to be similar, as this assumption does not influence the way the energy is focused inside the sample.
- The excitation and monitoring are realized on a line of nodes summed to extract a single A-Scan. This line is supposed to act as a longitudinal piezoelectric element. The distance between the nodes (0.4 μm) is small relative to the wavelength inside the converging lens (48 μm). Therefore, according to Huygens' principle, the sum of the nodes is equivalent to the sum of a surface.

Once again, these hypotheses are intended to reduce the time calculation which is critical. Even if the hypotheses are supposed to be correct, a comparison with experimental results is primordial in order to verify their effect.

3.2.4 Results

Figure 3.4 shows the wave propagation. The nodes corresponding to the piezoelectric element in the lens are excited along the y-axis (Figure 3.4 a.), then the acoustic beam is focused inside the water thanks to the converging lens (Figure 3.4 b.), a part of the energy is transmitted inside the sample and the rest is reflected in the water (Figure 3.4 c.). Finally, multiple reflections occur in the weld and propagate in the water up to the transducer (Figure 3.4 d.).

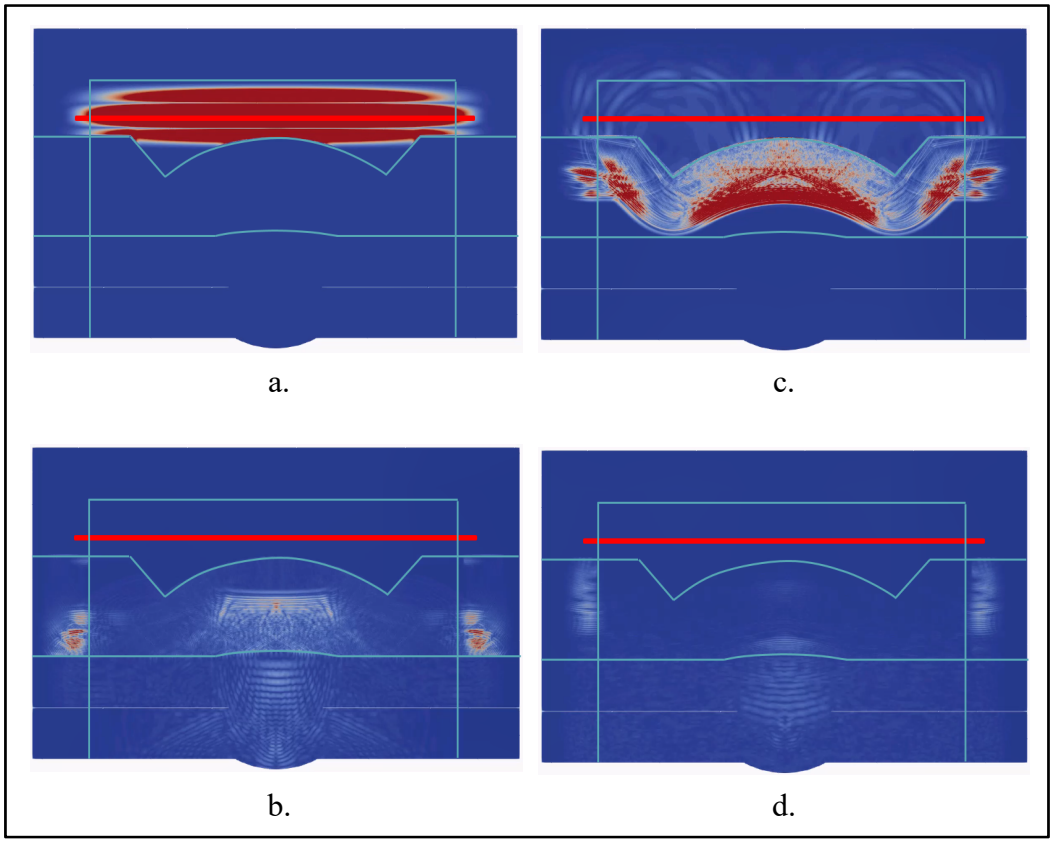

Figure 3.4 Wave propagation during a SAM measurement. a. Excitation. b. Focalization inside water. c. propagation inside the sample. d. Back propagation of signals towards the transducer

Combining the results of the 200 simulations with the weld moving along the x-axis, a B-Scan is formed in Figure 3.5. The right and the left-hand side of the image correspond to the regions where there are no features, only stainless steel plates. The middle (region with the bump) corresponds to the weld.

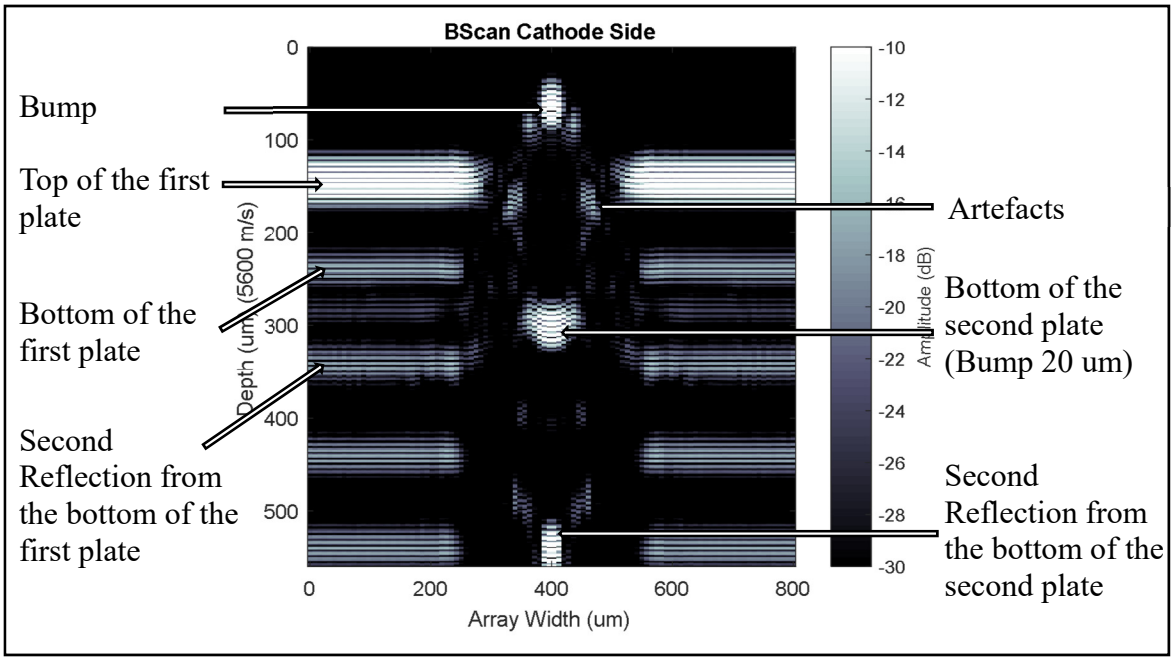

Figure 3.5 B-Scan image, result of simulations

The bump of the weld appears to be bigger on the B-Scan than it is in reality due to the difference in the speed of sound in stainless steel and water. Indeed, the sound propagates four times faster in steel than in water but the scale was realized using the sound velocity of stainless steel (5600 m/s). Therefore, the geometry of the surface is not right as the scale is generated with the wrong speed of sound. Thus, the bump appears to be four times bigger than it should be. The scale is only good for the features following the first echo as they correspond to features inside the stainless steel. However, the shift due to the bump remains for the features located below the bump.

Many double reflections occur inside the sample. In experimental tests, these double reflections should have lower amplitude as the material damping was not modelled in the simulations.

The sides of the weld bump have no amplitude because the slopes reflect the beam away from the transducer lens. Therefore, no amplitude is received when the transducer is above the slopes of the weld.

3.2.5 Simulations of defects

In order to identify any defect in the welds, several simulations were performed. The simulation presented above was a defect-free weld. A range of potential defects were modelled as shown in Figure 1.5. The model geometries and B-Scan results are shown in Figure 3.6.

Figure 3.6 b. c. and d. clearly show the internal defect in an identifiable way. However, the diagonal crack (Figure 3.6 a.) is particularly hard to detect because the defect is almost on the same axis as the propagation direction of the waves.

Figure 3.6 e. is a confirmation that the inclination is not an issue. Most of the plates investigated have some inclinations (4.5°) due to the general wrapping of the plates, which is affected by heat distortion of the welding. This effect does not affect the results.

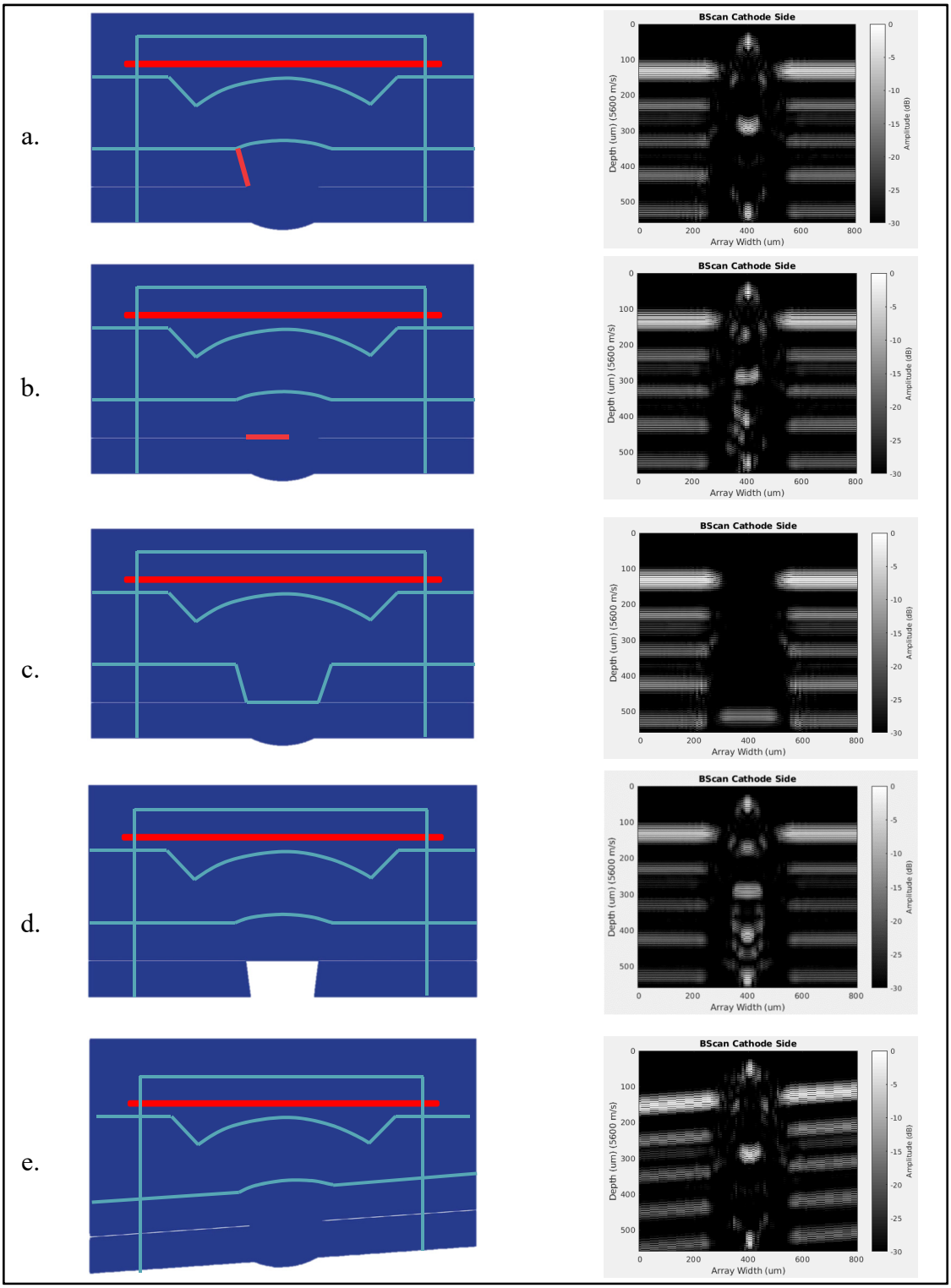

Figure 3.6 Simulations of defects. The model geometry is on the left and the B-Scan result is on the right. a. Diagonal crack. b. Horizontal crack. c. Hole on the cathode side. d. Hole on the anode side. e. Inclination of the sample

3.2.6 Conclusions on finite element simulations

The feasibility of the inspection was performed with 2-D FE simulations. Simulations of defect-free and defective welds showed the possibilities and limitations of laser weld inspection by SAM. All defects are recognizable except for diagonal cracks that are much harder to detect due to their direction. The inclination of the plates due to heat distortion during welding does not seem to affect the results. These promising results will now be validated against experiments.

3.3 Experimental tests

The last part of this project was to perform experimental tests to finally assess the feasibility of using SAM in order to find and characterize defects in thin laser welds.

Three SAM with different transducer configurations (focal distance, acoustic lens) were tested. Each of them had advantages and disadvantages. The first was a custom-made SAM located at the Riverside Research Institute of New York (Rohrbach, Lloyd, Silverman, & Mamou, 2015). The acoustic transducer was centred at 250 MHz and with a 450 μm curvature radius. However, the membrane was made of ZnO, which only allows low power to be transmitted. In the end, this setup did not allow signals to be received from the bottom of the samples because of the very short focal distance and the lack of power. The results of these first measurements will therefore not be presented in detail. The second and the third SAM were Nordson-Sonoscan Gen6 located at C2MI Bromont QC and Nordson-Sonoscan headquarters in Chicago, IL. The transducers used were both centred at 230 MHz with focal lengths of 6.35 mm and 3.81 mm respectively. Figure 3.7 shows the SAM during a scan on the BiP anode side.

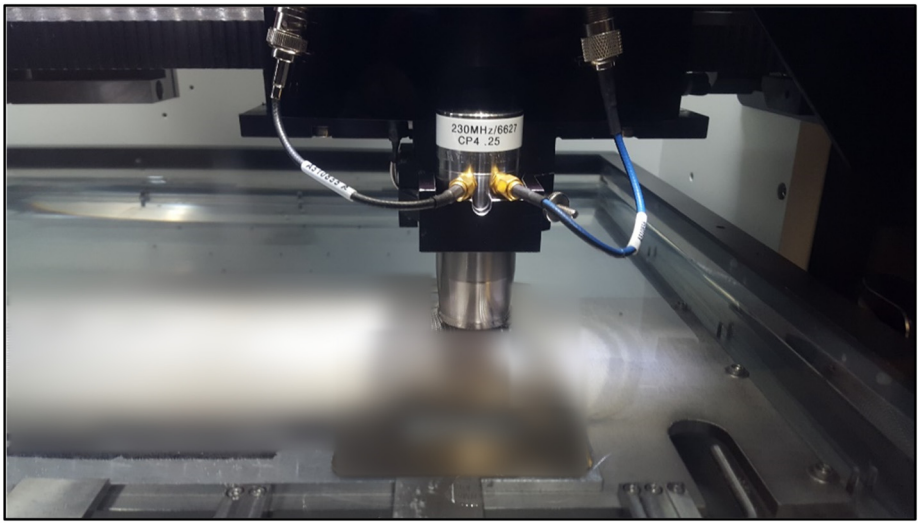

Figure 3.7 Picture of SAM during a scan on the BiP anode side. The picture is blurred for confidentiality reasons

The results presented below were all obtained with the third SAM (230 MHz, 3.81mm focal distance). The pixel pitch (lateral resolution) was 11 µm and the scan speed was 203.2 mm/s which means it takes approximately 5 minutes to image a 25x25 mm^2 zone.

3.3.1 Results on flawless welds

First, B-Scans from anode and cathode sides were performed in order to validate the simulations carried out in the previous section.

3.3.1.1 B-Scans

Two kinds of welds exist on the BiP: linear and spot welds. Both were measured in order to compare the simulations and experiments.

Figure 3.8 shows a linear weld B-Scan carried out on both sides of the BiP. The red line corresponds to the B-Scan width axis. The comparison between the simulation and experimental is shown in Figure 3.9.

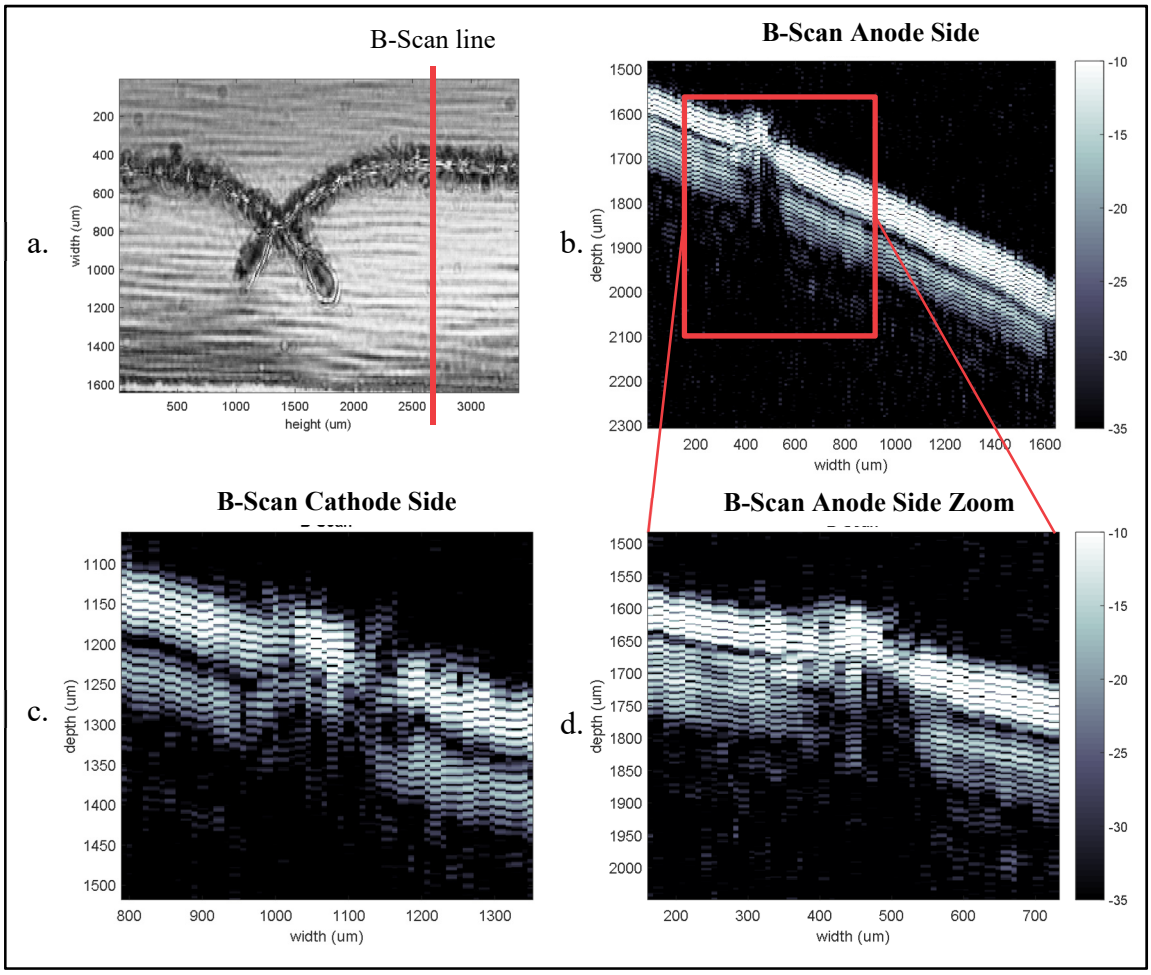

Figure 3.8 Experimental results on linear welds. a. Zone investigated (C-Scan image from the anode side). b. B-Scan of linear weld from the anode side. c. B-Scan images of the same position from the cathode side. d. Zoom of the B-Scan b.

The features of the simulations are present in the experiments. However, the measurements are not as clean as expected. The potential reasons for the differences are:

- The high attenuation inside the sample (barely any signal from the second reflection). The attenuation was not modelled in the simulations.
- The sample is far from flat, the distance between the transducer and the sample changes. This leads to changes in the position of the focal point and hence the amplitudes.
- The centre frequency shifts down, this problem is explained in the next paragraph.

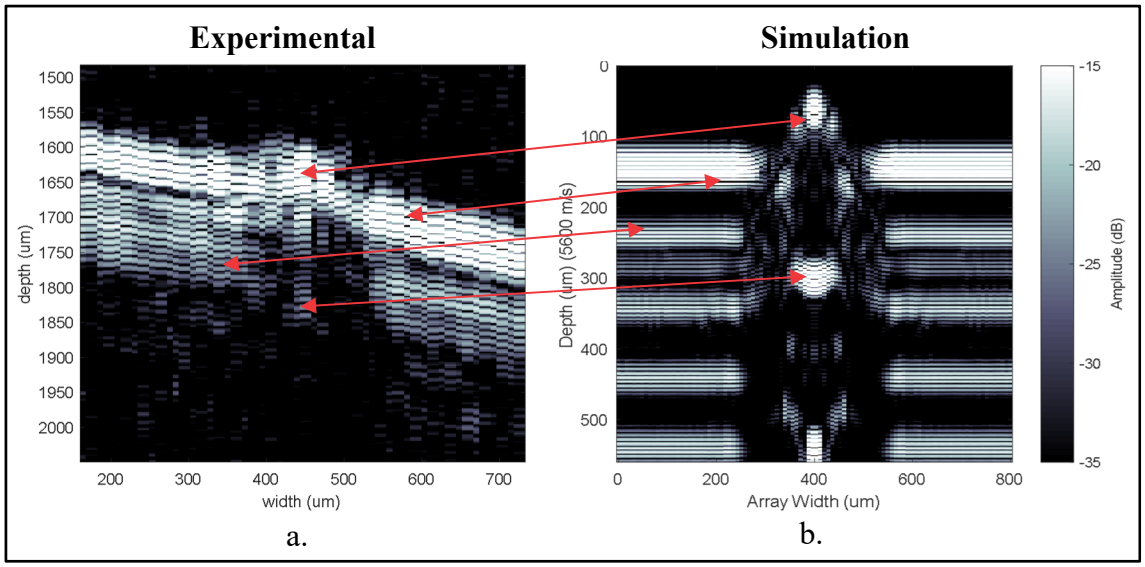

Figure 3.9 Comparisons between experimental (a.) and simulations (b.) B-Scans

3.3.1.2 Frequency shift issue

Frequency shift was a major issue that was not expected to be so important. The wavelength of the received signals was much longer than in the simulations. Figure 3.10 a. shows the received signal when the transducer is above a region of the plate without features. Figure 3.10 b. shows the FFT of this signal. The centre frequency is 120 MHz. However, the centre frequency of the transducer was 230 MHz and the excitation was performed at this frequency. This difference was due to attenuation in the water. Indeed, the attenuation is frequency dependent and it increases with the square of the frequency. Therefore, the higher frequencies are attenuated leading to a centre frequency shift. The distance travelled in the water is about 6 cm. Figure 3.11 shows the FFT of a simulated 5 cycle toneburst at 230 MHz with and without attenuation due to 6 cm of water. In practice the side lobes have less amplitude due to the transducer bandwidth. The phenomenon of the centre frequency shift was clearly identifiable.

The consequence was a reduction of the resolution along the z-axis. The signal coming back from the surface of the sample and the bottom of the first plate were supposed to be separated. But because of the shift, they were almost overlapped (Figure 3.9).

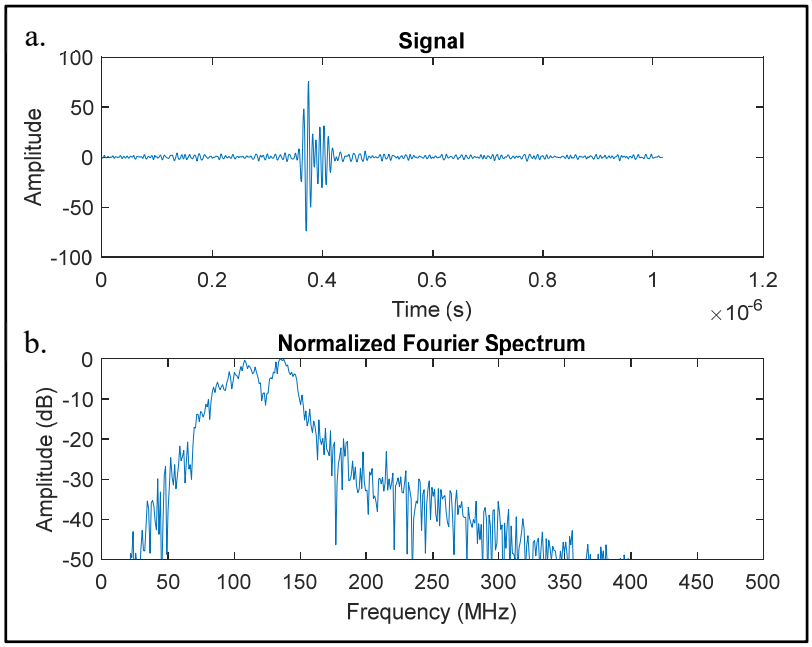

Figure 3.10 a. Received signal when the transducer is above a region of the plate without features. b. FFT of the signal

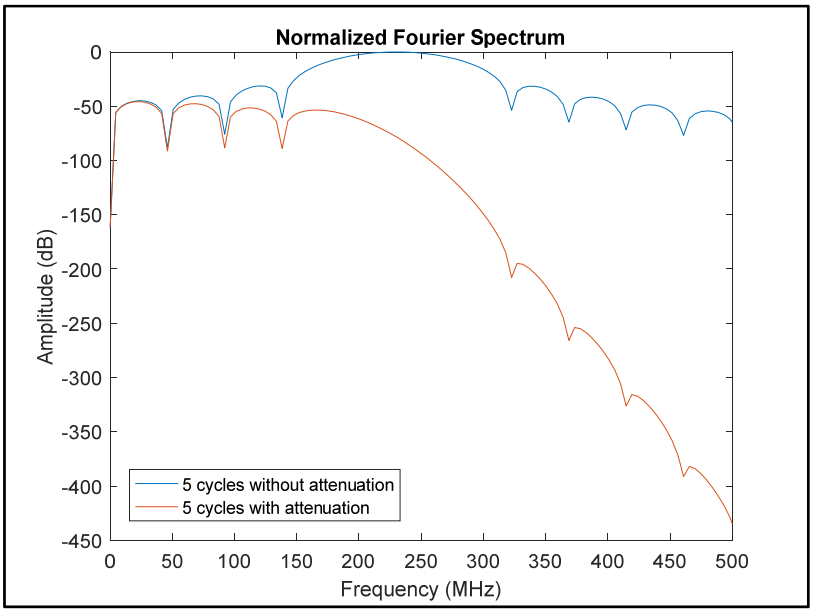

Figure 3.11 FFT of a 5-cycle toneburst at 230 MHz with and without the attenuation due to 6 mm of water

3.3.2 Results on welds with defects

This section concerns BiP with defective welds identified with the leakage test. The regions where the plates have external leaks (regions where bubbles appear during the leakage test) were known. The purpose of the measurements with the SAM was to identify the defective zones without a priori knowledge of their position. Once the zone was determined, the objective was to find the exact weld that causes the leakage and identify the defect by comparing with the simulations.

3.3.2.1 B-Scans

Figure 3.12 shows the comparison of two B-Scans measured from the cathode side. The first one (Figure 3.12 a.) is a good weld and the second (Figure 3.12 b.) is a bad one. The bad weld was identified using the leakage test. The defect of the bad weld seems to correspond to a horizontal crack. Indeed, the simulation of the defect (Figure 3.6 b.) corresponds to the experimental B-Scan (Figure 3.12 b.): a new spot appears between the spots corresponding to the top and the bottom of the weld.

It should be noted that B-Scans on spot welds have a better agreement with the simulations (the bottom of the weld is clearly identifiable). This is due to the geometry of the spot weld and the conic acoustic beam: more power penetrate to the bottom of the weld compared to linear weld thanks to the axisymmetric geometry of the spot welds.

A clear difference is visible between good and bad welds. Moreover, despite the fact that the images are not as clean as expected, some guesses on the defect nature can be made.

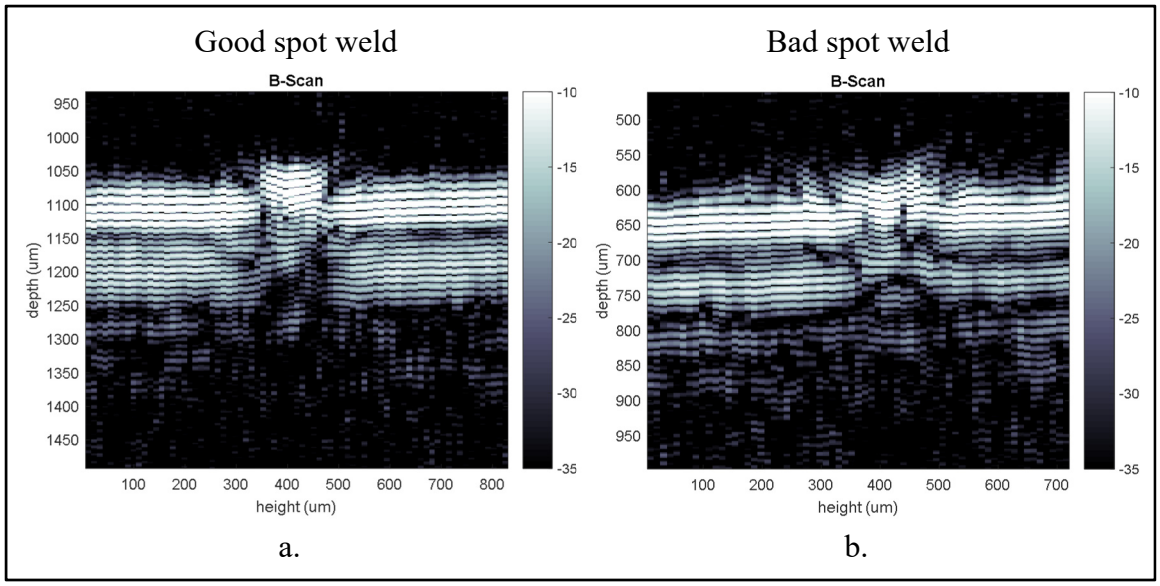

Figure 3.12 Comparison of two B-Scans measured from the cathode side. a. Good spot weld. b. Bad spot weld

3.3.2.2 C-Scans

Most of commercial SAM are aimed at making C-Scans as they are able to image larger regions and can easily highlight defects such as delamination. Figure 3.13 shows four C-Scans of the same region. Figure 3.13 (a. and c.) were taken from the cathode side and (b. and d.) from the anode side. The main difference was the location of the gate used. Indeed, for Figure 13 (a. and b.), the gate was located around the maximum amplitude received and with a width of 5 cycles (length of the first received signal). For Figure 3.13 (c. and d.) the gate had the same width but was located around 100 µm under the maximum received amplitude (surface). The gate was located at the bottom of the first plate.

Using a gate at -100 µm highlighted the defective spot welds (areas circled in red). Indeed, in Figure 3.13 (d) the spot welds behave like the plate meaning that there was a strong signal at -100 µm. However, if the welding was good, there would be no signal at this depth. Therefore, these welds were defective and the B-Scans can now be used in order to characterize the defect.

A good solution to highlight if the weld is going through or not would be to make C-Scans with a gate located around -230 µm. This corresponds to the distance between the top and the bottom of the weld. Therefore, if the weld was good, a spot would be expected at this depth. However, the bumps of the welds not always have the same size (changing the distance of 230 µm), thus the spot could be missed and incorrect conclusions would be made.

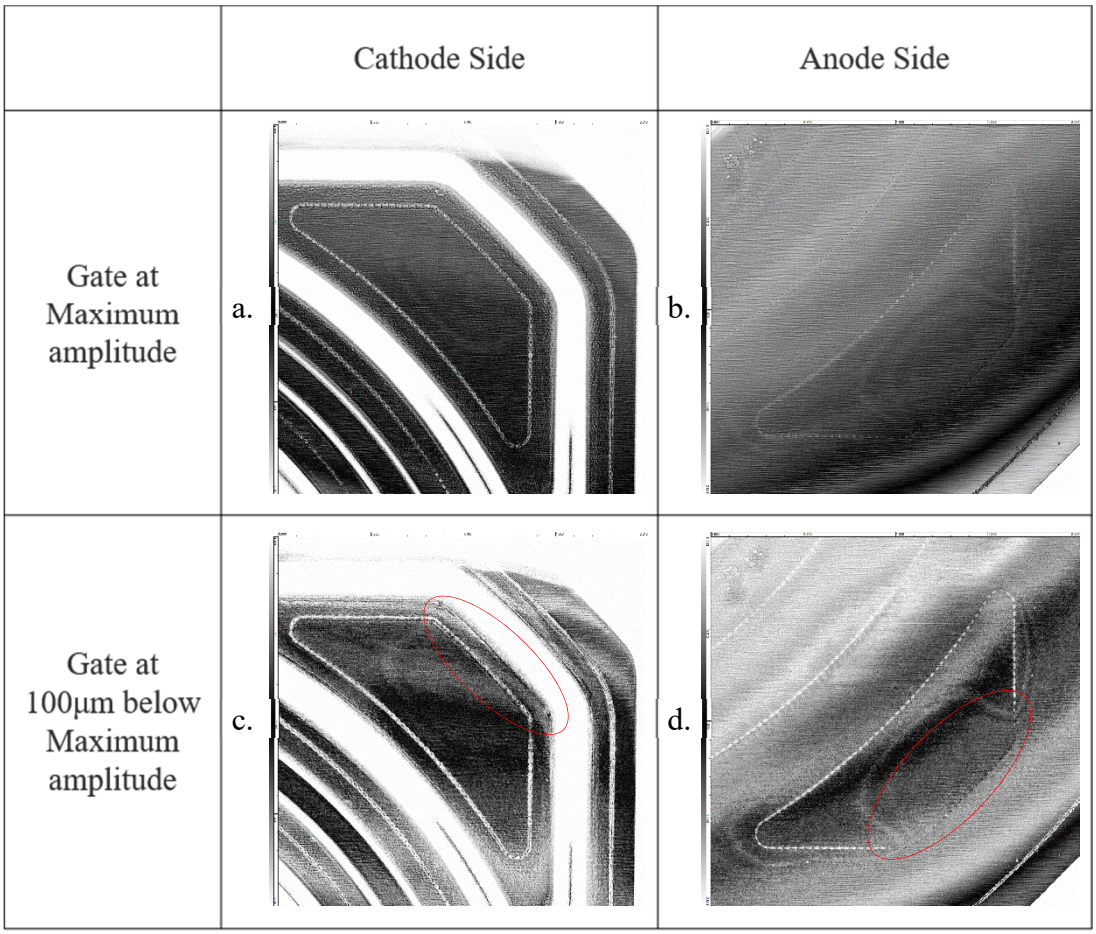

Figure 3.13 C-Scans of the same zone taken from the cathode and anode sides and with two different gate positions. The defective zone is circled in red. Image size: width 18 mm, length 18 mm

3.3.3 Discussions

Experimental results demonstrated and confirmed that SAM is a good way to point out defective areas on the BiP spot welds. However, the differences between simulations and

experiments were important. The reasons and potential improvements are detailed in this section.

3.3.3.1 Main issues

Measurements carried out with the SAM revealed many problems that were not identified during the simulations and that limit the accuracy of the inspection method. The potential reasons are:

- Center Frequency shift: lower centre frequency reducing the resolution along the depth (detailed in paragraph 3.3.1.2).
- High attenuation inside the sample. Indeed, there is barely any signal from the second reflection (see Figure 3.9 a.). Attenuation was not modelled in the simulations because experimental measurements were necessary in order to quantify the values to use.
- The sample is far from flat, the distance between the transducer and the sample changes. Figure 3.14 shows C-Scans of the same region considered defective thanks to the leak test. The scans were performed from the anode and the cathode sides with a gate at 100 µm below the maximum amplitude. The defective zone is identifiable (cf red circles). However, the image quality is very weakened by the grey level gradients. These gradients are due to the non-planarity of the plates caused by the pressurization of the plates during the leak test. This leads to changes in the position of the focal point and hence the amplitudes.
- The bumps of the welds are not as regular as expected which causes fluctuations in the echoes received.

Despite these problems, it was possible to locate the areas with defects, which answers part of the problem. However, it seems very difficult to identify the weld causing external leaks because of the problems mentioned above. However, some potential improvements presented in the next section could solve these issues.

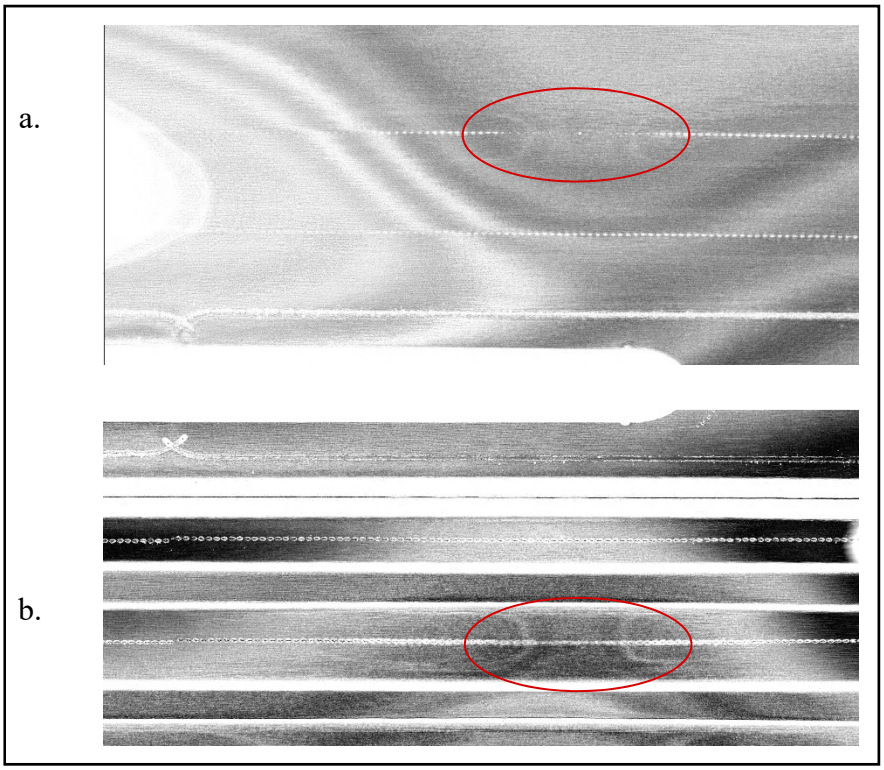

Figure 3.14 C-Scans of the same zone taken from the cathode and anode sides. Gates located at 100 µm below the maximum amplitude. Image size: width 18 mm, height 8 mm. a. Anode side. b. Cathode side

3.3.3.2 Potential improvements

Potential improvements to avoid or limit the problems described above:

- Using higher frequencies would improve the resolution along the z-axis. However, the attenuation would also be more important. Optimal frequency is to be determined.
- Bringing the transducer closer to the surface using a transducer with a shorter focal length (like the one at Riverside Institute but more powerful) would reduce the distance travelled in the water by the waves. Thus, attenuation in water would be reduced and the effect of the frequency shift would be decreased.
- Using a transducer with a larger bandwidth would reduce the number of cycles required and thus enhance the resolution along the z-axis.

- Changing the couplant can produce better results through better acoustic impedance matching and lower attenuation. However, other coupling agents are not as easy to use as water at room temperature.

3.4 Conclusion on the feasibility of the proposed method

Inspection of thin laser welds on stainless steel BiP by the use of SAM was investigated. The study was divided into two parts: FE simulations and experiments. A 2-D FE model containing all elements of the inspection (transducer, couplant and sample) was used in order to determine the feasibility of the inspection method. Simulations of good and defective welds showed the possibilities and limitations. All defects were recognizable except for diagonal cracks that are much harder to detect due to their direction. The second part had the objective of experimentally determining if the simulations were correct and concluding on the feasibility of inspecting welds with SAM. The experiments revealed many parameters that had not been taken into account for the simulations. Thus, the resolution of the real images was lower than simulated. Despite these problems, it is possible to locate the areas with defects, which answers part of the problem and potential improvements could be made.

CONCLUSIONS

The purpose of the study was to find an ultrasonic non-destructive technique in order to find and characterize defects in thin laser welds on stainless steel BiP of fuel cells. The width of these welds was approximately 200 µm. There are many NDT to inspect welds but none have been developed for such thin welds. Two solutions were investigated: GW and SAM.

The GW solution uses relatively low frequency (10 MHz) waves that propagate inside the plates towards the weld and interact with it. Depending on the properties of the waves back propagated, information on the weld can be deduced. The investigation was performed with FE simulations. The spatial energy distribution method showed no interest as no correlation was found between the width or Young's modulus of the weld and the energy partition between the branches. The pulse-echo method was more relevant as an image of the weld can be made. The lack of weld can be detected. However, this method was limited to this specific application and only works on continuous welds. Moreover, the geometry of the welds was complex and the space available between the welds and the features can be very narrow. Therefore, implementing this type of inspection would be highly complex.

The SAM solution uses much higher frequencies (230 MHz). A focused acoustic transducer fires a beam inside the sample and records the reflected signals. Thanks to motorized stages, the transducer fires and records the echoes over the entire surface of the sample. This study was divided into two parts: finite element simulations and experimental tests. The finite element simulations showed promising results as acoustic microscopes should be able to detect all defects except diagonal cracks. These simulations were very challenging due to the high frequency and the complex geometry of the transducer. The second part had the objective of experimentally determining if the simulations were correct and concluding on the feasibility of inspecting welds with SAM. The experiments revealed that many important parameters had not been taken into account in the simulations. Thus, the resolution of the real images was reduced compared to the simulated ones. Despite these problems, it was possible to locate the areas with defects, which addressed part of the problem. Moreover, potential improvements

could be made such as using higher frequencies, couplant with better impedance and attenuation properties, transducer with broader bandwidth and shorter focal distance. Another solution that could be useful to determine the location of the defects is transmission using two transducers on either side of the sample: one that transmits the signal and the second that receives on the other side. If the weld is defective, the received signal would change.

The SAM inspection method proved to be adequate to find defects in thin laser welds. However, to characterize those defects, further studies must be carried out in order to improve the resolution along the z-axis.

BIBLIOGRAPHY

Alleyne, D., & Cawley, P. (1991). A two-dimensional Fourier transform method for the measurement of propagating multimode signals. *The Journal of the Acoustical Society of America, 89*(3), 1159-1168.

Amphlett, J. C., Mann, R. F., Peppley, B. A., Roberge, P. R., & Rodrigues, A. (1996). A model predicting transient responses of proton exchange membrane fuel cells. *Journal of Power sources, 61*(1-2), 183-188.

Appleby, A. J. (1988). Fuel cell handbook.

Arone, M., Cerniglia, D., & Nigrelli, V. (2006). Defect characterization in Al welded joints by non-contact Lamb wave technique. *Journal of Materials Processing Technology, 176*(1-3), 95-101.

Blomen, L. J., & Mugerwa, M. N. (2013). *Fuel cell systems*. Springer Science & Business Media.

Briggs, A., Briggs, G., & Kolosov, O. (2010). *Acoustic microscopy* (Vol. 67). Oxford University Press.

Calmon, P., Mahaut, S., Chatillon, S., & Raillon, R. (2006). CIVA: An expertise platform for simulation and processing NDT data. *Ultrasonics, 44*, e975-e979.

Cawley, P., Lowe, M., Alleyne, D., Pavlakovic, B., & Wilcox, P. (2003). Practical long range guided wave inspection-applications to pipes and rail. *Mater. Eval, 61*(1), 66-74.

Che, S., Guduru, P., Nurmikko, A., & Maris, H. (2015). A scanning acoustic microscope based on picosecond ultrasonics. *Ultrasonics, 56*, 153-159.

Cheeke, J. D. N. (2016). *Fundamentals and applications of ultrasonic waves*. CRC press.

Chimenti, D. (1997). Guided waves in plates and their use in materials characterization. *Applied Mechanics Reviews, 50*(5), 247-284.

Comot, P., Bocher, P., & Belanger, P. (2017). Ultrasonic guided wave inspection of Inconel 625 brazed lap joints: Simulation and experimentation. *NDT & E International, 91*, 71-78.

Comsol, A. (2005). COMSOL multiphysics user's guide. *Version: September, 10*, 333.

Cook, R. D., Malkus, D. S., Plesha, M. E., & Witt, R. J. (1974). *Concepts and applications of finite element analysis* (Vol. 4). Wiley New York.

Ditchburn, R., Burke, S., & Scala, C. (1996). NDT of welds: state of the art. *NDT & E International, 29*(2), 111-117.

Dixon, S., Edwards, C., & Palmer, S. B. (1999). A laser–EMAT system for ultrasonic weld inspection. *Ultrasonics, 37*(4), 273-281.

Doctor, S., Hall, T., & Reid, L. (1986). SAFT—the evolution of a signal processing technology for ultrasonic testing. *NDT international, 19*(3), 163-167.

Drozdz, M., Moreau, L., Castaings, M., Lowe, M., & Cawley, P. (2006). Efficient numerical modelling of absorbing regions for boundaries of guided waves problems. Dans *AIP Conference Proceedings* (Vol. 820, pp. 126-133). AIP.

Drozdz, M. B. (2008). *Efficient finite element modelling of ultrasound waves in elastic media* (Imperial College London).

Farson, D., & Kim, K. (1999). Generation of optical and acoustic emissions in laser weld plumes. *Journal of applied physics, 85*(3), 1329-1336.

Fatemi, M., & Kak, A. C. (1980). Ultrasonic B-scan imaging: Theory of image formation and a technique for restoration. *Ultrasonic Imaging, 2*(1), 1-47.

Graff, K. F. (2012). *Wave motion in elastic solids*. Courier Corporation.

Grünwald, E., Hammer, R., Nuster, R., Wieser, P., Hinderer, M., Wiesler, I., . . . Brunner, R. (2017). Simulation of Acoustic Wave Propagation in Aluminium Coatings for Material Characterization. *Coatings, 7*(12), 230.

Holmes, C., Drinkwater, B., & Wilcox, P. (2004). The post-processing of ultrasonic array data using the total focusing method. *Insight-Non-Destructive Testing and Condition Monitoring, 46*(11), 677-680.

Holmes, C., Drinkwater, B. W., & Wilcox, P. D. (2005). Post-processing of the full matrix of ultrasonic transmit–receive array data for non-destructive evaluation. *NDT & E International, 38*(8), 701-711.

Huthwaite, P. (2014). Accelerated finite element elastodynamic simulations using the GPU. *Journal of Computational Physics, 257*, 687-707.

ISO, E. (2007). 6520-1. *Welding and allied processes-Classification of geometric imperfections in metallic materials-Part 1: Fusion welding*.

Katayama, S. (2013). *Handbook of laser welding technologies*. Elsevier.

Krautkrämer, J., & Krautkrämer, H. (2013). *Ultrasonic testing of materials*. Springer Science & Business Media.

Li, L., Brookfield, D., & Steen, W. (1996). Plasma charge sensor for in-process, non-contact monitoring of the laser welding process. *Measurement Science and Technology, 7*(4), 615.

Long, R., Russell, J., & Cawley, P. (2012). Ultrasonic phased array inspection using full matrix capture. *Insight-Non-Destructive Testing and Condition Monitoring, 54*(7), 380-385.

Maev, R. G. (2008). *Acoustic microscopy: Fundamentals and applications*. John Wiley & Sons.

Mountford, R., & Wells, P. (1972). Ultrasonic liver scanning: the A-scan in the normal and cirrhosis. *Physics in Medicine & Biology, 17*(2), 261.

Niedrach, L. W. (1964). Fuel cell: Google Patents.

Peng, L., Yi, P., & Lai, X. (2014). Design and manufacturing of stainless steel bipolar plates for proton exchange membrane fuel cells. *International journal of hydrogen Energy, 39*(36), 21127-21153.

Rajagopal, P., Drozdz, M., Skelton, E. A., Lowe, M. J., & Craster, R. V. (2012). On the use of absorbing layers to simulate the propagation of elastic waves in unbounded isotropic media using commercially available finite element packages. *NDT & E International, 51*, 30-40.

Rohrbach, D., Lloyd, H. O., Silverman, R. H., & Mamou, J. (2015). Fine-resolution maps of acoustic properties at 250 MHz of unstained fixed murine retinal layers. *The Journal of the Acoustical Society of America, 137*(5), EL381-EL387.

Rose, J. L. (2004). *Ultrasonic waves in solid media*. Cambridge university press.

Rose, J. L. (2014). *Ultrasonic guided waves in solid media*. Cambridge university press.

Sforza, P., & de Blasiis, D. (2002). On-line optical monitoring system for arc welding. *NDT & E International, 35*(1), 37-43.

Shao, J., & Yan, Y. (2005). Review of techniques for on-line monitoring and inspection of laser welding. Dans *Journal of Physics: Conference Series* (Vol. 15, pp. 101). IOP Publishing.

Tanter, M., & Fink, M. (2014). Ultrafast imaging in biomedical ultrasound. *IEEE transactions on ultrasonics, ferroelectrics, and frequency control, 61*(1), 102-119.

Tiran, E., Deffieux, T., Correia, M., Maresca, D., Osmanski, B.-F., Sieu, L.-A., . . . Tanter, M. (2015). Multiplane wave imaging increases signal-to-noise ratio in ultrafast ultrasound imaging. *Physics in Medicine & Biology, 60*(21), 8549.

Tommiska, O., Mäkinen, J., Meriläinen, A., Hyvönen, J., Nolvi, A., Ylitalo, T., . . . Hæggström, E. (2018). Multiphysics Simulation of a High Frequency Acoustic Microscope Lens. *Microscope, 23*, 2.

Trots, I., Nowicki, A., & Lewandowski, M. (2009). Synthetic transmit aperture in ultrasound imaging. *Archives of Acoustics, 34*(4), 685-695.

Wilcox, P., Evans, M., Diligent, O., Lowe, M., & Cawley, P. (2002). Dispersion and excitability of guided acoustic waves in isotropic beams with arbitrary cross section. Dans *AIP Conference Proceedings* (Vol. 615, pp. 203-210). AIP.

Wilcox, P. D. (2003). Omni-directional guided wave transducer arrays for the rapid inspection of large areas of plate structures. *IEEE transactions on ultrasonics, ferroelectrics, and frequency control, 50*(6), 699-709.

Yan, F., & Rose, J. L. (2007). Guided wave phased array beam steering in composite plates. Dans *Health Monitoring of Structural and Biological Systems 2007* (Vol. 6532, pp. 65320G). International Society for Optics and Photonics.

Yu, X., Zuo, P., Xiao, J., & Fan, Z. (2019). Detection of damage in welded joints using high order feature guided ultrasonic waves. *Mechanical Systems and Signal Processing, 126*, 176-192.

Zhang, J. (2008). *PEM fuel cell electrocatalysts and catalyst layers: fundamentals and applications*. Springer Science & Business Media.

Zhang, Y., Kovacevic, R., & Li, L. (1996). Characterization and real-time measurement of geometrical appearance of the weld pool. *International Journal of Machine Tools and Manufacture, 36*(7), 799-816.

Zhenhua, C., Shi, Y., & Zhao, H. (2008). Evaluating technology of spot weld quality for coated high strength steel sheet based on ultrasonic guide wave. Dans *2008 IEEE Ultrasonics Symposium* (pp. 406-409). IEEE.